Distribution of hydrated minerals in the north polar region of Mars

B. H. Horgan,[1] J. F. Bell III,[1] E. Z. Noe Dobrea,[2] E. A. Cloutis,[3] D. T. Bailey,[3] M. A. Craig,[3] L. H. Roach,[4] and J. F. Mustard,[4]

Received 9 May 2008; revised 9 September 2008; accepted 4 November 2008; published 28 January 2009.

[1] The previous discovery of extensive deposits of hydrated minerals in Olympia Planum in the north polar region of Mars by the Mars Express OMEGA instrument raises important questions about the origin and subsequent redistribution of these hydrated minerals. Here we present a new map of the distribution of hydrated minerals within the north polar region of Mars by applying both standard and new spectral analysis techniques to near-infrared spectral data from OMEGA. Our results are in agreement with the previous OMEGA observations but also show more extensive detections of hydrated minerals throughout the circumpolar plains, as well as new detections of hydrated minerals on the surface of Planum Boreum and within the polar troughs. We find that while the circumpolar plains hydration signatures appear to be correlated with the dark dunes of the north polar erg, hydration signatures in Planum Boreum instead appear to be correlated with the north polar veneers and their sources within the polar layered deposits. By applying laboratory-derived empirical models of the dependence of gypsum spectra on grain size and abundance, we provide approximate abundance estimates for the hydrated minerals we have identified in Observatoire pour la Minéralogie, l'Eau, les Glaces et l'Activité (OMEGA) and Compact Reconnaissance Imaging Spectrometer (CRISM) data. We find that the presence of hydrated minerals throughout the north polar region suggests (1) a complex cycle of sediment exchange between the Olympia Planum dunes and the other polar units; (2) an earlier origin for the hydrated minerals than originally postulated; and (3) the occurrence of significant water activity in this region during the Amazonian.

Citation: Horgan, B. H., J. F. Bell III, E. Z. Noe Dobrea, E. A. Cloutis, D. T. Bailey, M. A. Craig, L. H. Roach, and J. F. Mustard (2009), Distribution of hydrated minerals in the north polar region of Mars, *J. Geophys. Res.*, *114*, E01005, doi:10.1029/2008JE003187.

1. Introduction

[2] The north polar region of Mars is situated at the lowest elevation within a basin that encompasses much of the northern hemisphere, making it an ideal place for the potential deposition of outflow channel fluids and sediments [*Fishbaugh and Head*, 2000; *Tanaka*, 2005; *Tanaka et al.*, 2008]. Today, dark-toned sedimentary structures dominate the nonice regional geology. Dark-toned sediments make up the large, aeolian dune fields and sand sheets in the circumpolar plains (the north polar erg) between about 75°N and 85°N (Figure 1) [*Tsoar et al.*, 1979; *Thomas and Weitz*, 1989; *Lancaster and Greeley*, 1990], while on Planum Boreum, dark-toned sediments are present within the polar layered deposits and on the surface as water ice-free, low-albedo surfaces, classified as the north polar veneers [e.g., *Rodriguez et al.*, 2007; *Tanaka*, 2005; *Malin and Edgett*, 2001]. Evidence in the region for large, aqueous outflows from the ice cap [*Fishbaugh and Head*, 2002], volatile-driven resurfacing [*Tanaka et al.*, 2003; *Wyatt et al.*, 2004], and water-equivalent hydrogen contents of the subsurface in excess of 30% by mass [*Feldman et al.*, 2004] suggest that, in addition to aeolian processes, surface or groundwater may have played a role in the formation and modification of these deposits. Consequently, the composition, morphology, and current physical state of the dark-toned sedimentary deposits may give insight into surface deposition and modification processes in the north polar region, throughout, or even prior to, the Amazonian.

[3] Results from the Mars Express spacecraft's Observatoire pour la Minéralogie, l'Eau, les Glaces et l'Activité (MEx/OMEGA) near-IR imaging spectrometer investigation [*Bibring et al.*, 2004] have indicated the presence of extended deposits of hydrated calcium sulfates in the Olympia Planum region [*Langevin et al.*, 2005a], possibly implying an important role for surface or near-surface water in the alteration of the dune materials. *Langevin et al.* [2005a] proposed that the observed hydrated calcium sulfates are gypsum ($CaSO_4 \bullet 2H_2O$) on the basis of comparison with spectra taken by OMEGA during ground calibration. Gypsum can be formed in a variety of environments, but in general, gypsum formation requires a source of sulfur and H_2O (in the liquid or gas phase) interacting with Ca-bearing minerals. *Langevin et al.*

[1]Department of Astronomy, Cornell University, Ithaca, New York, USA.
[2]JPL, California Institute of Technology, Pasadena, California, USA.
[3]Department of Geography, University of Winnipeg, Winnipeg, Manitoba, Canada.
[4]Department of Geological Sciences, Brown University, Providence, Rhode Island, USA.

Copyright 2009 by the American Geophysical Union.
0148-0227/09/2008JE003187

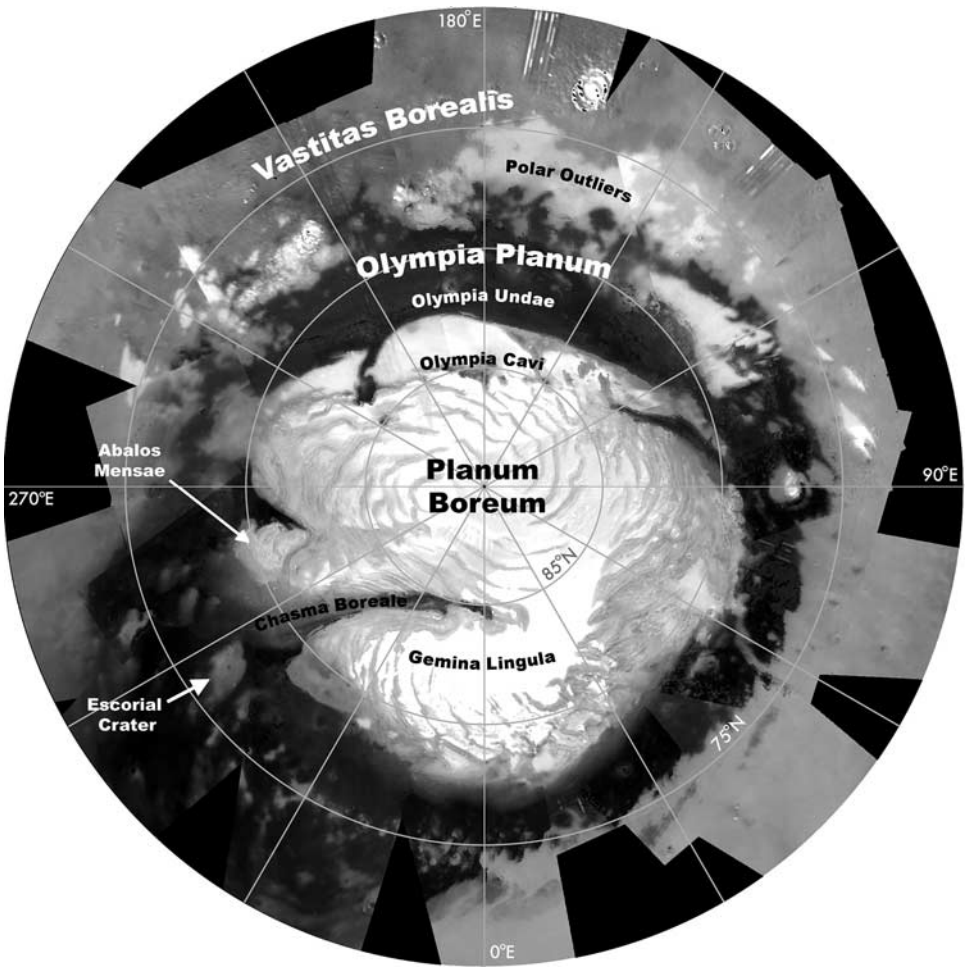

Figure 1. OMEGA 0.9-1.1 μm average estimated Lambert albedo mosaic of the 45 early northern summer image cubes used in our study (Table 1), stretched between 0.1 and 0.6. Geographic names mentioned in text are indicated.

[2005a] further suggested that the water necessary to form gypsum was most likely present in or near Olympia Planum owing to outflows from the ice cap during a warm climate excursion, but did not propose a source for sulfur-rich material. *Fishbaugh et al.* [2007] reported that although the gypsum deposit is nearly exclusively associated with the dark dunes, there were no apparent correlations between the presence of gypsum and the physical or thermal characteristics of the dune field in the THEMIS data included in their study. Those authors proposed that the water necessary for gypsum formation emanated from the ice cap during a purported Chasma Boreale melting event [*Fishbaugh and Head*, 2002] or during an impact melting event in the region near the highest gypsum concentrations. Alternatively, *Tanaka* [2006] and *Tanaka et al.* [2008] argued that there is no clear geologic evidence for polar outflows during the Amazonian. Instead, they proposed that the Scandia geologic unit may consist of volcanic or hydrothermal deposits, and that the gypsum may be sourced directly from this older (early Amazonian) unit. Indeed, deposition of large quantities of sulfates since the emplacement of the young (late Amazonian), transient dune fields does not easily fit within the OMEGA global hypothesis of sulfate deposition during the Hesperian [*Bibring et al.*, 2006].

[4] In this study, we examine hydration in the entire north polar region to establish a regional context for the Olympia Planum sulfates, to test the proposed OMEGA global mineralogic history in the region, and to propose additional or alternate hypotheses to explain the observed mineral distributions and their geologic/stratigraphic context. If the sulfates are limited to Olympia Planum, then they may be intimately related to the dunes and much younger than sulfate deposits elsewhere on Mars; alternately, hydrated minerals associated with older deposits elsewhere in the region may suggest less recent water activity in the region and a possible source for the gypsum from older deposits.

[5] This mapping effort differs from previous OMEGA and Mars Reconnaissance Orbiter/Compact Reconnaissance Imaging Spectrometer (MRO/CRISM) mapping efforts [*Langevin et al.*, 2005a; *Roach et al.*, 2007; *Pelkey et al.*, 2007] because we have developed a technique (described in section 4.2) that allows us to search for hydrated minerals in water ice-rich areas, which previously have not been examined. By using this new technique, we have been able to verify the OMEGA sulfate detection as well as to expand on the OMEGA results with a more detailed search for other hydrated deposits in the region. In addition, our ongoing laboratory studies of potential mineralogies for the hydrated

deposits, using newly available laboratory sulfate mineral spectra [e.g., *Cloutis et al.*, 2006], have allowed us to provide a new assessment of the abundance of hydrated minerals in the region.

[6] In this study, we have employed a range of data sets in addition to the OMEGA spectral data to analyze the distribution of hydrated minerals, including geologic and morphologic maps of the north polar region [*Tanaka et al.*, 2008; *Tanaka*, 2005; *Rodriguez et al.*, 2007; *Tanaka and Hayward*, 2008] high-resolution spectral data from CRISM, altimetry data from the Mars Global Surveyor/Mars Orbiter Laser Altimeter (MGS/MOLA) [*Zuber et al.*, 1992, *Smith et al.*, 2001], and visible wavelength images from the MRO Context Camera (CTX) [*Malin et al.*, 2007], the MRO High Resolution Imaging Science Experiment (HiRISE) [*McEwen et al.*, 2007], and the Mars Odyssey orbiter's Thermal Emission Imaging System (ODY/THEMIS) [*Christensen et al.*, 2004a].

[7] In section 2, we provide an overview of the geologic units and features of the north polar region, with an emphasis on Olympia Planum. In section 3, we describe the compositional properties of Olympia Planum, provide a background on terrestrial gypsum deposition, and describe previous hypotheses for deposition of the Olympia Planum gypsum. Section 4 details the methods we used to verify the OMEGA sulfate detection and to produce a new map of the distribution of hydrated minerals, and section 5 presents our spectral maps as well as correlations between our maps and other data sets. Section 6 describes our efforts to model the abundances of gypsum in both CRISM and OMEGA observations using laboratory data, and section 7 presents our interpretations of our findings in the context of the regional geologic history.

2. Regional Geologic Units

[8] The north polar region of Mars exhibits a complex and dynamic geologic history that extends through the Amazonian. In this section, we provide an overview of previous work on the regional geologic units, with an emphasis on the history and current state of the north polar erg.

2.1. Pre-MGS Geologic Interpretations

[9] The smoother surfaces and lower crater densities as compared to the southern highlands observed in the northern basin since Mariner 9 has suggested that the northern basin was resurfaced at some point in Martian history [e.g., *Scott and Carr*, 1978], but what processes did the resurfacing and when it happened has only become apparent in more recent mapping efforts. The availability of higher-resolution images and other data sets has steadily decreased the apparent age of the north polar basin materials from the Noachian-Hesperian ages interpreted from Mariner 9 data [*Scott and Carr*, 1978], to the Hesperian-Amazonian ages interpreted from Viking data, [*Dial*, 1984; *Scott and Tanaka*, 1987], and more recently, to the exclusively Amazonian ages interpreted from MGS and ODY data [*Tanaka et al.*, 2003, 2008; *Tanaka*, 2005]. The inferred source and nature of the materials has also changed dramatically. During the Viking era, the materials filling the northern basin, or the Vastitas Borealis Formation (VBF), were interpreted as Hesperian volcanic flows with varying degrees of degradation [e.g., *Scott and Tanaka*, 1987]. With higher-resolution images from MGS and ODY, the VBF is currently interpreted as late Hesperian outflow sediments that have been extensively reworked by periglacial processes since the early Amazonian [e.g., *Tanaka*, 2005].

2.2. Recent Geologic Interpretations

[10] According to recent geologic mapping [*Tanaka*, 2005; *Tanaka et al.*, 2008], the geology of the north polar region can be described by distinct units separated in time and space, as shown in Figure 2. In the plains, the Vastitas Borealis interior and Scandia region units have been mapped as having been emplaced during the early Amazonian by sediments from catastrophic outflows originating at lower latitudes, and reworking of those sediments by phreatic processes such as mud volcanism. The Rupes Tenuis unit is superposed unconformably on top of the plains units, and is interpreted to have most likely formed by redeposition of sediment from the previously much more extensive Scandia unit. The Rupes Tenuis unit makes up the terrace-forming, stratigraphically lowest section of the layers previously classified as the polar basal unit [*Edgett et al.*, 2003; *Fishbaugh and Head*, 2005], and has a maximum observed thickness of ~1300 m [*Tanaka et al.*, 2008]. An extended period of erosion during the Middle Amazonian may have considerably reduced the size of the Rupes Tenuis unit, which, in the plains, may have left behind impact-cemented plateaus such as those exposed at the mouth of Chasma Boreale and in the nearby Escorial pedestal crater plateau [*Tanaka et al.*, 2008].

[11] *Tanaka et al.* [2008] have classified the upper section of the basal unit as the Planum Boreum cavi unit, which formed from many episodes of sand deposition, and has been described as a paleoerg deposit [*Byrne and Murray*, 2002; *Fishbaugh and Head*, 2000, 2001, 2005; *Tanaka*, 2005]. Major geologic evidence for the paleoerg includes the cross-bedded nature of the Planum Boreum cavi unit and the unit's tendency to be thickest in depressions in the Rupes Tenuis unit [*Tanaka et al.*, 2008]. Additionally, the Planum Boreum cavi unit appears to make up the bulk of the topography of Olympia Planum, which suggests that Olympia Planum may have a long history of aeolian activity.

[12] The Planum Boreum 1 unit, which makes up the bulk of the lower polar layered deposits, unconformably overlies the Planum Boreum cavi unit, and exhibits up to ~1500 m of even, fine layering, most likely composed of air fall deposits [*Blasius et al.*, 1982; *Fishbaugh and Head*, 2005; *Malin and Edgett*, 2001; *Milkovich and Head*, 2005, 2006; *Tanaka*, 2005; *Tanaka et al.*, 2008]. The emplacement of the Planum Boreum 1 unit was followed by another extensive period of erosion, during which katabatic winds may have first carved the spiral troughs that are now being exposed throughout Planum Boreum, potentially by similar processes [*Tanaka et al.*, 2008].

[13] Following the period of erosion, the troughs were subsequently filled in by ~100 m of dark sediments that now comprise the Planum Boreum 2 unit [*Rodriguez et al.*, 2007; *Tanaka et al.*, 2008]. The Planum Boreum 2 unit makes up the lowest portion of the upper layered deposits or "banded terrain" [*Howard et al.*, 1982; *Tanaka*, 2005], and appears to be composed of ice-free sand and dust, which is mobilized to form the extensive low-albedo surfaces that mantle much of the periphery of Planum Boreum (Figure 1) [*Rodriguez et al.*, 2007]. The low-albedo surfaces are thick enough to obscure or partially obscure the spectral signature of the water ice below, but not to obscure the underlying morphology, leading

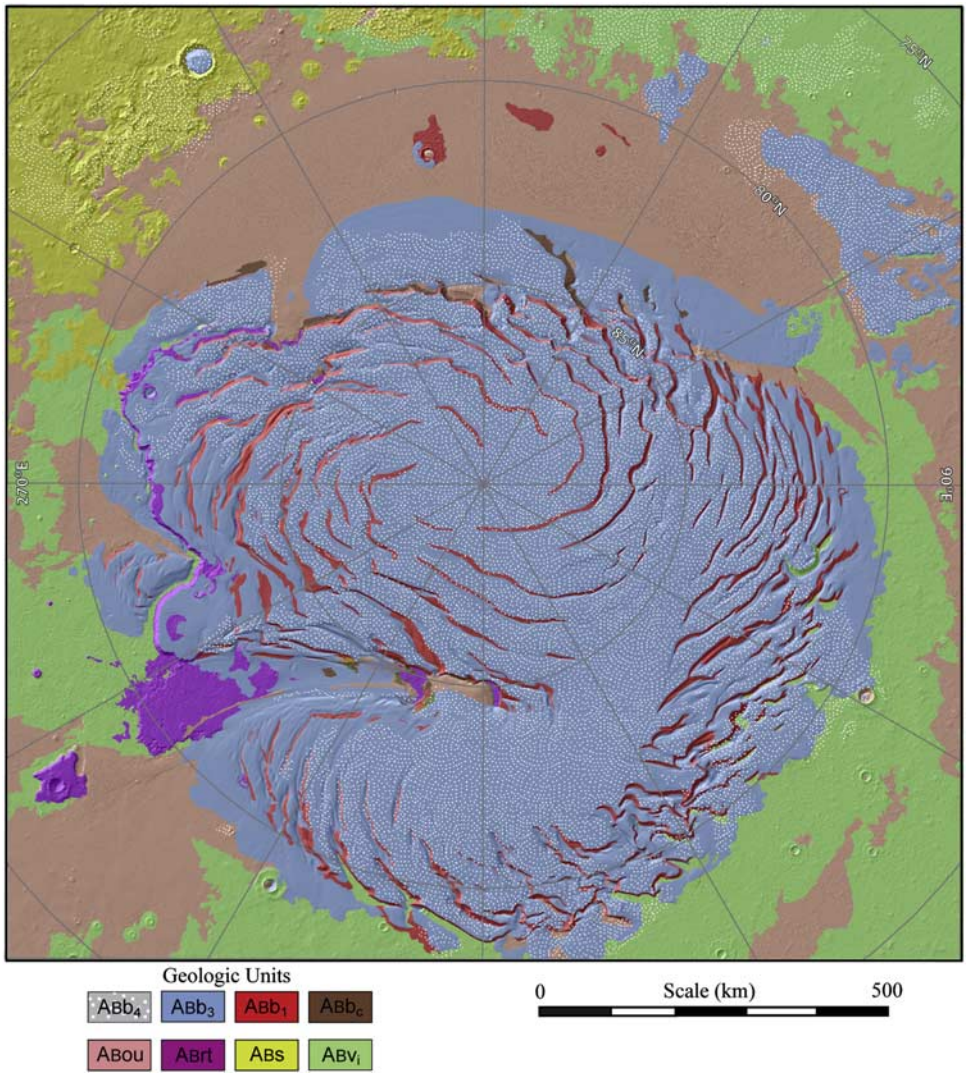

Figure 2. Geologic map of the north polar region, after *Tanaka et al.* [2008]. Units indicated in legend and in text are the Planum Boreum units 1–4 (ABb_{1-4}), Planum Boreum cavi unit (ABb_c), Olympia Undae unit (ABou), Rupes Tenuis unit (ABrt), Scandia region unit (ABs), and Vastitas Borealis interior unit (ABv_i).

Rodriguez et al. [2007] to classify these low- albedo deposits as "veneers." The veneers are associated with grooves and striations in the residual cap, implying a highly mobile and abrasive particle component, and exhibit variations in albedo indicative of multiple episodes of formation. The older, lighter toned veneers may be indurated by water ice or hydrated minerals. *Rodriguez et al.* [2007] also speculate that the dark layers within the Planum Boreum 1 and 3 units may be remnants of paleoveneers.

[14] The uppermost units of Planum Boreum are the shallow, but extensive, Planum Boreum 3 and 4 units. The Planum Boreum 3 unit makes up the bulk of the upper layered deposits mapped by *Tanaka* [2005], covers all Planum Boreum surfaces except for equatorward trough walls and trough floors, and is also found mantling dunes around the periphery of Planum Boreum. Additionally, HiRISE images have shown the Planum Boreum 3 unit present as bright deposits in interdune areas in Olympia Planum [*Roach et al.*, 2007]. The Planum Boreum 4 unit is composed of the young, bright residual ice cap on Planum Boreum and the polar outliers, and exhibits high surface water ice concentrations in OMEGA and initial CRISM studies [*Langevin et al.*, 2005b; *Seelos et al.*, 2007].

2.3. Olympia Planum and the Circumpolar Erg

[15] The Olympia Planum erg (Olympia Undae) is the largest aeolian accumulation on Mars, with a surface area of 4.7×10^6 km^2 [*Lancaster and Greeley*, 1990]. For scale, this is slightly larger than the state of California, and 150% larger than the Rub al Khali, Saudi Arabia, the largest active erg on Earth [*Tsoar et al.*, 1979]. As shown in Figure 1, Olympia Undae extends in latitude from 80°N to 85°N, and follows the edge of the residual water ice cap from 140°E to 240°E, with an 800 m topographic high above the adjacent plains near 180°E [*Tanaka*, 2005; *Tanaka et al.*, 2008]. The remainder of the circumpolar erg and associated sand sheets encircle the

rest of Planum Boreum [e.g., *Tanaka and Hayward*, 2008], and while the sand sheets exhibit a marked albedo difference compared to the underlying plains (Figure 1), they may only be a few grains thick in many areas [*Tanaka et al.*, 2008].

[16] Using terrestrial relationships between dune spacing and sediment volume, *Lancaster and Greeley* [1990] estimated the volume of sediment contained in Olympia Undae at around 900 km^3, compared to approximately 1150 km^3 in the entire circumpolar erg. Using MOLA data, *Zuber et al.* [1998] estimated the volume of sediment in the circumpolar erg to be approximately 10,000 ± 3000 km^3, although it is unclear what criteria were used to determine dune coverage or individual dune volume in that study. More recently, *Hayward et al.* [2008], in initial mapping of the dune density throughout the north polar region using THEMIS, MOC, and CTX images, have found 835,000 km^2 of terrain with some type of dune coverage. As shown by *Tanaka and Hayward* [2008], dune density decreases with distance from Olympia Planum and Chasma Boreale.

[17] Previous workers have proposed that the current source of the dark dune material in Olympia Undae is the lower, platy unit of the polar layered deposits or basal unit [*Thomas and Weitz*, 1989; *Byrne and Murray*, 2002; *Fishbaugh and Head*, 2005]. In recent geologic mapping, the current source unit has been identified as the Planum Boreum cavi unit, the stratigraphically oldest Planum Boreum unit characterized by alternating layers of cross-bedded, unconsolidated, dark-toned, dune forming materials and light-toned boulder forming materials [*Tanaka et al.*, 2008]. Although the dunes appear to be actively sourced from this unit today, the Olympia Undae unit has most likely formed episodically throughout the Amazonian, and may have originally formed as a result of the erosion of the Rupes Tenuis and Scandia region units [*Tanaka et al.*, 2008].

[18] Much of the Olympia Undae unit appears to be stabilized, as indicated by mantling of many dune fields by the Planum Boreum 3 unit and the north polar veneers (section 5.4) [*Tanaka*, 2005; *Tanaka et al.*, 2008], as well as by the presence of induration features on dunes, including surface cracks, absence of dry grain flow on avalanche faces, avalanche remnants in interdune areas [*Feldman et al.*, 2008], slumps, yardangs, craters, thick dust coverings, and avalanche chutes [*Schatz et al.*, 2006]. In addition, many of the dunes exhibit muted forms, and have not been observed to move (on the scale of meters) in the 30 years between Viking and MOC observations [*Schatz et al.*, 2006]. *Feldman et al.* [2008] have suggested, on the basis of modeling of Mars Odyssey Neutron Spectrometer (MONS) data, that the dunes have water ice-rich cores, overlain by a mobile layer on the order of ~10 cm thick. The water ice-rich cores may be similar to terrestrial niveoaeolian deposits, which are composed of interbedded sand, dust, and water ice or snow, are more resistant to erosion than ice-free dunes, and would account for the overall lack of movement and muted forms. However, it must be noted that even spatially deconvolved MONS data have a 300 km footprint [*Feldman et al.*, 2008], so it is unclear how input from Planum Boreum and the surrounding terrains would affect models of the water ice content of Olympia Undae. Exceptions to the overall stabilized nature of the dune fields include dunes that are associated with dark, downwind streaks, possibly indicative of recent sand movement [*Tanaka et al.*, 2008], and two dunes that have been observed to shrink and disappear over ~3 years of MOC observations [*Bourke et al.*, 2008].

3. Composition of Olympia Undae

[19] The dunes of Olympia Undae exhibit the strongest and most areally extensive hydrated sulfate signature yet seen on Mars [e.g., *Poulet et al.*, 2007]. In this section, we review the initial sulfate detection by OMEGA and CRISM, the previously proposed gypsum deposition mechanisms, and proposed mafic mineralogies for the dunes.

3.1. Olympia Undae Sulfates

[20] *Langevin et al.* [2005a] first announced the unambiguous detection of hydrated Ca-sulfates in Olympia Undae, by the observation of a strong absorption band at 1.9 μm, indicating hydration, accompanied by several less pronounced bands between 1.0 and 2.5 μm diagnostic of Ca-sulfates, interpreted to be indicative of gypsum. Mapping the band depth of the 1.9 μm feature throughout the north polar region revealed that the signature was largely restricted to the dunes, with the largest band depth located near the eastern margin of Olympia Undae, near 80.2°N, 244.5°E [*Langevin et al.*, 2005a]. *Fishbaugh et al.* [2007] expanded on the initial OMEGA detection by presenting several regions with putative gypsum signatures outside the main dune field, including a region beyond the eastern dune margin, as well as a localized region on the floor of Chasma Boreale. *Fishbaugh et al.* [2007] also identified a lack of hydrated mineral signatures in the exposed unit between Planum Boreum and Olympia Undae, which they interpreted as indicating that the gypsum is not sourced from the Planum Boreum units.

[21] *Fishbaugh et al.* [2007] modeled the bulk composition of the sulfate-rich dunes as a mixture of gypsum grains and an unknown dark, spectrally featureless (DSF) material. An intimate mixture model of the two components yielded a best fit to the OMEGA data for 55% DSF with a grain size of a few tens of μm mixed with 45% gypsum with grain sizes between 100 μm and 1 mm. A better fit was found using an intramixture model, where oxide grains are housed as inclusions in larger gypsum grains. The model yielded a best fit with 35% pure gypsum grains with particle sizes of a few tens of μm and 65% mm-sized gypsum grains contaminated with DSF inclusions. *Fishbaugh et al.* [2007] favored the latter model because of the ability of the DSF inclusions to mask the high albedo of the gypsum grains, as well as to mask the large band depth that a nearly pure, coarse-grained gypsum dune would exhibit [e.g., *Cloutis et al.*, 2006]. The models did not include any specifically basaltic materials.

[22] The north polar region was a primary target for initial MRO observations after the spacecraft arrived in mid northern summer. In total, 6 targeted CRISM observations were located in Olympia Undae, with the goal of characterizing the distribution of gypsum within the dunes [*Roach et al.*, 2007]. Initial results indicate that CRISM data appear to confirm the gypsum detection, and show high gypsum band depths along the crests of dunes in the gypsum-rich area (section 6.1), which, when considered with the apparent aeolian distribution of the gypsum westward in Olympia Undae, suggests a dynamic process controlling the gypsum distribution [*Roach et al.*, 2007].

3.2. Gypsum Deposition Mechanisms and Properties

[23] Three principal solid phases occur in the calcium sulfate-water system: $CaSO_4 \bullet 2H_2O$ (gypsum), $CaSO_4 \bullet 0.5\ H_2O$ (bassanite), and $CaSO_4$ (anhydrite) [e.g., *Deer et al.*, 1992]. Of these three, only gypsum and anhydrite are stable phases; however, anhydrite is only dominant in water above 44°C on Earth at standard pressure and neutral pH, although the stability temperature decreases as pressure increases [*Deer et al.*, 1992; *Holland and Malinin*, 1979]. With the exception of environments involving such high-temperature waters, anhydrite is generally considered to be a secondary mineral assemblage to gypsum, although reforming gypsum through hydration of anhydrite is possible [*Deer et al.*, 1992].

[24] As a dry solid, gypsum is stable up to temperatures of 70°C at standard pressure, at which point bassanite is generated. Above 200°C, anhydrite is generated [*Deer et al.*, 1992; *Holland and Malinin*, 1979]. Gypsum is not stable under burial of more than a few hundred meters, at which point anhydrite is generated, with a volume loss of ~50% [*Schreiber and El Tabakh*, 2000]. Solid gypsum also dehydrates to anhydrite when exposed to high salinity solutions [*Deer et al.*, 1992].

[25] Gypsum has been shown to be stable at Martian surface pressures for periods of a few months on the basis of spectral analysis [*Cloutis et al.*, 2007]. This result can most likely be expanded to much longer time scales, as the structural integrity of gypsum is dependent on the presence of H_2O, and would require either extreme pressure excursions (down to a few Pa) or modest thermal input to dehydrate, as discussed above [*Cloutis et al.*, 2007].

[26] On Earth, gypsum is the most common sulfate mineral, and is most often associated with shallow and deep marine precipitate deposits as well as coastal (sabkha or salina) and continental (playa) evaporite deposits [*Schreiber and El Tabakh*, 2000; *Warren*, 1982]. Typical seawater contains approximately 0.15% dissolved $CaSO_4$, which equals about 1.7 cm precipitated gypsum per 100 m of evaporated seawater [*Deer et al.*, 1992; *Holland and Malinin*, 1979]. Gypsum is generally the second mineral to precipitate from evaporating seawater, after calcite [*Spencer*, 2000; *Holland and Malinin*, 1979]; however, highly acidic conditions that are plausible to have occurred on Mars may have inhibited carbonate deposition [e.g., *Catling*, 1999; *Fishbaugh et al.*, 2007]. In shallow marine environments, gypsum is most often deposited as crusts and clusters, while in deep marine environments, gypsum is most often deposited as fine grained beds, known as alabaster gypsum [*Schreiber and El Tabakh*, 2000].

[27] In salinas and playas, gypsum is present as (1) gypsite, a fine grained (<60 μm) gypsum crust dissolved and redeposited by rain, (2) gypsarenite, sand-sized (60 μm-1 mm) gypsum crystals deposited in unstable or periodic salinity environments, and (3) selenite, large (>2 mm) and often twinned gypsum crystals deposited below the water table in a continuously subaqueous environment [e.g., *Warren*, 1982]. Gypsum may also occur as a continental evaporite when it is dissolved in and transported by percolating groundwater, which is pulled to the surface by capillary action, depositing gypsarenite, selenite, and anhydrite crystals as the water evaporates [*Deer et al.*, 1992; *Langford*, 2003].

[28] Gypsum may also be formed without the presence of surface water. Sulfuric acid solutions moving through Ca-rich rocks may result in gypsum and anhydrite deposition. Such waters are often either created by volcanic gases interacting with meteoric water or by weathering of sulfides [*Deer et al.*, 1992; *Holland and Malinin*, 1979]. Ferric sulfate formation via weathering of sulfides has been shown to be plausible on Mars on the basis of mineral assemblages at the Viking landing sites [e.g., *Burns*, 1987, 1988; *Burns and Fisher*, 1990, 1993]. Likewise, gypsum and anhydrite rich mineral assemblages are often produced by the action of sulfurous volcanic vapors on Ca-rich rocks [e.g., *Golden et al.*, 2005]. These assemblages are commonly found in fumarole deposits [e.g., *Stoiber and Rose*, 1974]. Finally, gypsum can also be produced by sulfurous fog acting on Ca-rich materials [e.g., *Eckardt and Schemenauer*, 1998; *Golden et al.*, 2005].

[29] Gypsum is an especially weak mineral (hardness ~2) [*Deer et al.*, 1992], and likely would not survive for long as intact grains under the high saltation velocities that are postulated to occur on Mars [e.g., *Sagan et al.*, 1977]. Even under the much slower saltation velocities of Earth, gypsum sand at the White Sands dune field, NM has been observed to decrease in grain size with distance from the gypsum source [; *Ghrefat et al.*, 2007; S. G. Fryberger, Geological overview of White Sands National Monument, available online at http://www.nps.gov/archive/whsa/Geology%20of%20White%20Sands/GeoHome.html, 2002]. This may imply that the gypsum source region must be near the highest concentration of gypsum in eastern Olympia Planum [*Fishbaugh et al.*, 2007].

3.3. Gypsum Deposition Hypotheses

[30] *Langevin et al.* [2005a] initially proposed a suite of gypsum deposition mechanisms, including (1) atmospheric weathering of iron sulfides, (2) the interaction of Ca-rich rocks with acidic snow during a period of extensive volcanic activity, (3) sulfate-rich groundwater sourced from basal melting of Planum Boreum, or (4) hypersaline, sulfate-rich surface water sourced from polar outflows. *Fishbaugh et al.* [2007] evaluated several possible water-related gypsum deposition mechanisms and supported the hypothesis for gypsum deposition via the direct interaction of hypersaline, sulfate-rich surface water from a polar outflow. They proposed that the sulfur-rich outflow emanated from Chasma Boreale and traveled hundreds of kilometers through channels running along the base of Planum Boreum to a putative gypsum source area that today is ringed by dunes with a minor gypsum component. However, the channels identified in MOLA topography have alternately been interpreted as the result of erosion by katabatic winds off of Planum Boreum [*Warner and Farmer*, 2007]. Additionally, outflows from Planum Boreum would most likely be directed into the large basin to the south of Hyperborea Lingula, which in turn would have been dissected by such flood events occurring during the Amazonian, which is not observed [*Tanaka*, 2006].

[31] Alternatively, *Tanaka* [2006] proposed that the sulfate deposit is not late Amazonian in origin, but is rather considerably older than the dunes. In this hypothesis, the sulfates were originally generated by volcanically introduced sulfur and hydrothermal alteration of Ca-bearing volcanic rocks in the Scandia region and extending north to Olympia Planitia

due to magmatic intrusions propagating from Alba Patera during the early Amazonian. The dunes of Olympia Undae would not have been involved in the deposition of the sulfates in this model, but rather would have exposed the sulfates from the substrate via aeolian excavation [*Tanaka*, 2006; *Tanaka et al.*, 2008]. This hypothesis is supported by the presence of features suggestive of mud volcanism, pingo-like extrusions, and phreatic or cryoclastic eruptions in the Scandia unit [*Tanaka et al.*, 2003; *Tanaka*, 2005].

[32] One of the most puzzling aspects of the question of deposition mechanisms for the sulfate deposit is the timing of deposition. On the basis of OMEGA and Mars Express High Resolution Stereo Camera (HRSC) observations, the most widespread period of sulfate genesis in and around the Valles Marineris region may have been during the early to mid-Hesperian [*Bibring et al.*, 2006]. If the Olympia Planitia gypsum was created by the interaction of some form of H_2O with the Olympia Undae dunes, and the dunes are in fact Amazonian in age, then the north polar sulfate deposit does not correlate with the putative ages of sulfate deposits elsewhere. However, if the dunes are not involved in the genesis of the sulfates, and instead the sulfates are sourced from a much older unit, then this aspect of the geologic history of the north polar region may be more consistent with the *Bibring et al.* [2006] interpretation of the geologic history of Mars and the *Tanaka* [2006] hypothesis for gypsum exhumation.

3.4. Olympia Undae Ferrous Materials

[33] Aeolian bed forms on Mars are dominantly composed of dark sand grains, which are basaltic in composition based on remote sensing and in situ observations [e.g., *Bell et al.*, 2004; *Bibring et al.*, 2005; *Christensen et al.*, 2000, 2004b; *Gellert et al.*, 2004; *Morris et al.*, 2006; *Rogers and Aharonson*, 2008]. Previous workers have classified the Olympia Undae dunes as the lowest albedo and lowest thermal inertia dune field on the planet [*Thomas and Weitz*, 1989; *Herkenhoff and Vasavada*, 1999], possibly implying that the erg has undergone unique processes and has a distinct composition as compared to other Martian dune fields.

[34] *Bell et al.* [1997] identified a strong 953 nm absorption restricted to the circumpolar dark deposits in near-infrared Hubble Space Telescope (HST) multispectral images of the north polar region, implying a strong mafic component to the dunes, most likely a pyroxene. Initial analysis of TES observations by *Noe Dobrea and Bell* [2001] also suggested a strong pyroxene component to the dunes. OMEGA observations have suggested minor amounts of pyroxene in Olympia Planum [*Fishbaugh et al.*, 2007]; however, these detections are largely confined to localized areas outside the main dune field.

[35] Olympia Undae has since been identified as one of the strongest TES surface type 2 (ST2) [*Wyatt et al.*, 2004] signatures on the planet [*Ruff and Christensen*, 2007]. TES ST2 may be a primary volcanic lithology or an alteration product, possibly in the form of a rind. *Wyatt* [2007] have suggested that the differences between the elemental chemistry implied by deeper-probing Mars Odyssey Gamma Ray Spectrometer data and the TES observations in the northern plains implies that the TES ST2 is a surface coating. Although the exact mineralogy of TES ST2 is still in question, intermediate plagioclase and/or a high silica amorphous phase are strong candidates [*Ruff and Christensen*, 2007].

4. Methods

4.1. Data Calibration and Reduction

[36] Tools designed by the OMEGA team for basic calibration of OMEGA data are available on the European Space Agency's Planetary Science Archive Web site (http://www.rssd.esa.int/index.php?project=PSA). We have used the SOFT03 package, released in October 2005. This package contains IDL programs for extracting raw data, calibrated (I/F) data, and associated calibration information [*Bellucci et al.*, 2006]. We have developed in-house tools for sorting candidate image cubes, removing bad spectels (spectral pixels), removing the solar and atmospheric spectral contributions, creating mapped polar mosaics, and calculating band depth, as discussed below.

[37] A recurrent problem in the majority of these image cubes is the presence of planes of bad pixels 15 pixels wide in the horizontal spatial coordinate, between columns 81 and 96. The bad pixels are either saturated or null, and are confined to alternating pixels in the vertical spatial direction in a fairly consistent pattern (electronic error) [*Bellucci et al.*, 2006]. For the sake of continuity in our final mosaic, we have removed the bad pixels by replacing each bad pixel with the average of pixels above and below at every wavelength, producing a relatively seamless image without significant spectral errors.

[38] To compensate for atmospheric absorption, we have employed an atmospheric absorption model based on the model created by the OMEGA team [*Langevin et al.*, 2005a; E. Z. Noe Dobrea et al., manuscript in preparation, 2009]. In this model, the opacity of the atmosphere between 1.1 and 2.5 μm was empirically derived from the ratio of OMEGA spectra of high and low elevation regions on Olympus Mons (20.9 km and −2.8 km altitude above the ellipsoid), specifically from image ORB0479_5. The atmospheric spectrum for each pixel was then derived by modeling the surface spectrum between 1.954 and 2.010 μm (within the strong CO_2 bands) as a function of the atmospheric opacity and applying the derived model to the rest of the spectrum. Because the 2 μm CO_2 bands vary with atmospheric pressure, the model accounts for elevation changes [*Langevin et al.*, 2005a; E. Z. Noe Dobrea et al., manuscript in preparation, 2009]. Unfortunately, atmospheric spectra created using this method do not accurately model the strong upper atmospheric "hot bands" centered at 1.911 μm and 2.177 μm, as the bands are removed in the ratio. Fortunately, these bands are narrow enough that they only strongly affect one spectel, and we remove them by interpolating across each spectel.

[39] We have applied this model to the OMEGA spectra taken with the short-wavelength infrared channel (SWIR), which includes our wavelengths of interest between 0.93 and 2.5 μm. We have assumed that atmospheric gas opacity has had little effect on spectra taken with the visible and near-infrared channel (VNIR), which includes wavelengths between 0.38 and 1.05 μm, and have not applied a correction to the spectra in that range. Because the spectra overlap at 1.1 μm, we have combined the two spectral ranges by scaling nonatmospherically corrected VNIR spectra to match the value of the atmospherically corrected SWIR spectra at 1.1 μm.

Table 1. Properties of Images in Our OMEGA Spectral Mosaic

Image Cube	Center Latitude (°N)	Center Longitude (°E)	Maximum Resolution[a] (km/pixel)	Minimum Resolution (km/pixel)	L_s (°)
ORB1054_3	78.7	53.7	1.59	2.49	114.5
ORB1076_3	82.6	46.6	1.60	2.48	117.4
ORB1047_3	77.7	25.7	1.60	2.49	113.6
ORB1072_3	81.9	81.9	1.60	2.49	116.8
ORB1043_3	77.3	62.6	1.60	2.49	113.1
ORB1007_3	71.0	4.0	1.60	2.49	108.5
ORB1069_3	81.5	19.6	1.60	2.49	116.4
ORB1070_3	81.3	276.1	1.60	2.49	116.6
ORB1029_3	74.7	357.4	1.60	2.50	111.3
ORB1081_3	83.3	269.8	1.61	2.50	118.0
ORB1083_3	83.7	72.5	1.61	2.49	118.3
ORB1092_2	84.9	256.0	1.62	2.49	119.4
ORB0915_2	71.6	44.8	2.47	3.73	96.9
ORB0902_2	69.4	242.4	2.47	3.74	95.3
ORB1056_2	82.6	92.3	2.47	3.61	114.8
ORB0912_2	71.0	338.5	2.47	3.73	96.5
ORB0909_2	70.8	286.5	2.47	3.78	96.1
ORB1043_2	84.6	299.3	2.48	3.62	113.1
ORB1065_2	81.1	282.5	2.48	3.62	115.9
ORB1041_2	85.2	134.9	2.48	3.62	112.8
ORB1066_2	81.0	183.9	2.48	3.62	116.1
ORB1032_2	85.8	320.5	2.48	3.62	111.7
ORB0955_2	78.6	67.3	2.48	3.73	101.9
ORB1034_2	85.6	120.1	2.48	3.62	111.9
ORB1030_2	85.9	161.6	2.48	3.62	111.4
ORB0946_2	77.1	233.8	2.48	3.73	100.8
ORB1029_2	85.4	265.1	2.48	3.63	111.3
ORB1040_2	84.9	240.6	2.48	3.62	112.7
ORB0927_2	74.0	306.0	2.48	3.73	98.4
ORB0930_2	74.5	8.8	2.48	3.74	98.8
ORB1037_2	85.5	177.2	2.48	3.62	112.3
ORB0934_2	74.9	332.6	2.48	3.74	99.3
ORB0973_2	81.6	91.5	2.48	3.73	104.2
ORB1001_1	78.9	88.3	3.60	4.79	107.7
ORB1022_1	75.3	180.8	3.60	4.80	110.4
ORB1007_1	77.9	217.2	3.60	4.79	108.5
ORB1015_1	76.7	147.1	3.60	4.79	109.5
ORB1008_1	77.6	121.4	3.61	4.80	108.6
ORB0961_1	84.1	78.9	3.71	4.90	102.6
ORB0965_1	83.6	41.9	3.71	4.90	103.1
ORB0946_1	85.2	124.8	3.71	5.11	100.8
ORB0941_1	85.7	265.4	3.72	5.12	100.1
ORB0888_1	82.6	161.3	3.72	5.33	93.5
ORB0887_1	82.1	255.8	3.72	5.35	93.4
ORB0886_1	80.4	4.9	3.72	4.91	93.3

[a]Resolutions calculated from SWIR telescope resolution (~1.2 mrad) [*Bibring et al.*, 2004] and slant distance from spacecraft to each pixel.

[40] To correct for viewing angle and obtain an estimate of the surface albedo, we have applied a Lambertian phase function correction to the OMEGA data by dividing the spectra by the cosine of the incidence angle for each pixel. Although a Lambertian correction may not be the most appropriate or rigorous treatment for the surface phase function [e.g., *Soderblom et al.*, 2006; *Bell et al.*, 2008], it is the simplest solution to implement, given the uncertainties in the derivation of viewing angles for each pixel and our lack of understanding of the photometric properties of the variety of surfaces that we are observing in this region. Our mineralogic interpretations discussed below do not depend critically on the details of this photometric correction.

4.2. Spectral Mapping

[41] The OMEGA image cubes that we have used in this study have resolutions between 1.5 and 5.4 km/pixel, lie north of 70°N, and are limited to L_S between 90° and 115°. We have chosen this time range in order to acquire data after the summer solstice (to minimize the presence of surface CO_2 and H_2O frost), but before the onset of the summer north polar hood (to minimize the presence of water ice clouds). Of these, we have chosen a subset of 45 OMEGA image cubes to map in the north polar region. These 45 were chosen for maximum coverage and quality of data (see Table 1 for properties of the image cubes).

[42] To analyze these observations, we first mapped the 45 image cubes in a polar stereographic mosaic with a resolution of 1 km/pixel and a southern extent of 70°N. The resolution of the OMEGA image cubes varies from cube to cube as well as within each cube, so mapping the data to a constant resolution map requires interpolation of the lowest-resolution data. As such, the resolution of our final mosaic and the maps produced from it is higher than that of many of the observations, which may be as low as 5 km/pixel (see Table 1). The amount of interpolation involved in mapping 5 km/pixel

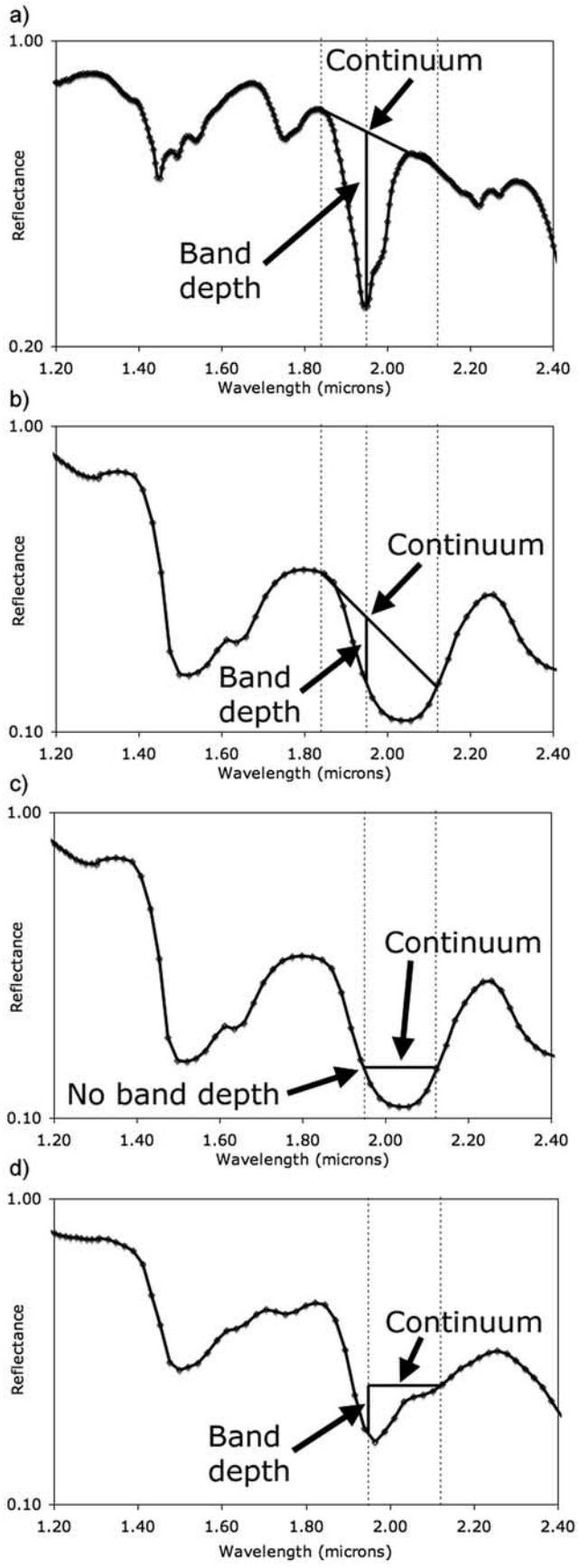

resolution data to a 1 km/pixel resolution map could potentially cause artificial mixing of spectra at interfaces between spectrally distinct terrains. To decrease the amount of interpolation that occurs at interfaces between terrains with and without hydration signatures, our mapping method is biased toward images with higher hydration band depths (see section 4.3), which means that our maps incorporate data with the least amount of mixing at interfaces. Boundaries between spectrally distinct terrains are accurate to within the original resolution of the data, on the order of 2 km in most cases.

[43] Hydrated minerals are primarily identified by the presence of the 1.9 μm molecular H_2O overtone absorption band, and the depth of that band can be used as a proxy for mineral abundance [*Hunt and Salisbury*, 1970; *Cloutis et al.*, 2006]. The standard approach for evaluating the 1.9 μm hydration band depth is shown in Figure 3a, and is expressed by the following equation, where *R(x)* is the reflectance at wavelength *x*:

$$BD(1.934) = 1 - R(1.934) \Big/ \left(\left(\frac{R(2.122) - R(1.842)}{2.122 - 1.842} \right) \cdot (1.934 - 1.842) + R(1.842) \right) \quad (1)$$

By fitting a linear continuum between a spectrum's values at 1.842 and 2.122 μm, the 1.934 μm band depth of that spectrum can be evaluated as the difference between the spectrum and the continuum at that wavelength, expressed as a percentage [e.g., *Clark and Roush*, 1984]. The precise minimum of the 1.9 μm band is at 1.944 μm [*Cloutis et al.*, 2006], so ideally, we should use the 1.941 μm OMEGA spectral channel; however, because atmospheric absorption is much less at 1.927 than at 1.941 ($\sim$2% versus $\sim$10%) [*Langevin et al.*, 2005a], we are averaging the 1.927 and 1.941 μm channels for a potentially less atmospheric-dependent band depth. This offset from the band center may slightly underestimate the band depth.

[44] This approach yields deceptive results in areas with surface H_2O ice. Water ice has broad absorption bands at 1.5 and 2.0 μm, which vary strongly in depth as a function of water ice grain size [*Clark*, 1981b]. Because the 2 μm water ice band overlaps with the 1.9 μm hydration band, using the standard approach to identify the presence of a 1.9 μm hydration band yields a false positive in the presence of water ice, as shown in Figure 3b. The solution used in previous mapping efforts with OMEGA and CRISM data has been to exclude icy regions from the maps [*Poulet et al.*, 2007; *Pelkey et al.*, 2007]. An alternate solution that we describe

Figure 3. Schematic evaluation of the 1.9 μm hydration band depth relative to the continuum value at 1.84 and 2.12 μm for (a) gypsum [*Cloutis et al.*, 2006], yielding positive detection of the hydration band and (b) water ice [*Roush et al.*, 1990], yielding a positive band depth but ultimately a false detection of the hydration band. Schematic evaluation of the 1.9 μm hydration band depth relative to symmetric wavelengths across the 2.03 μm ice band, near 2.1 μm for (c) water ice and (d) an equal linear mixture of water ice and gypsum.

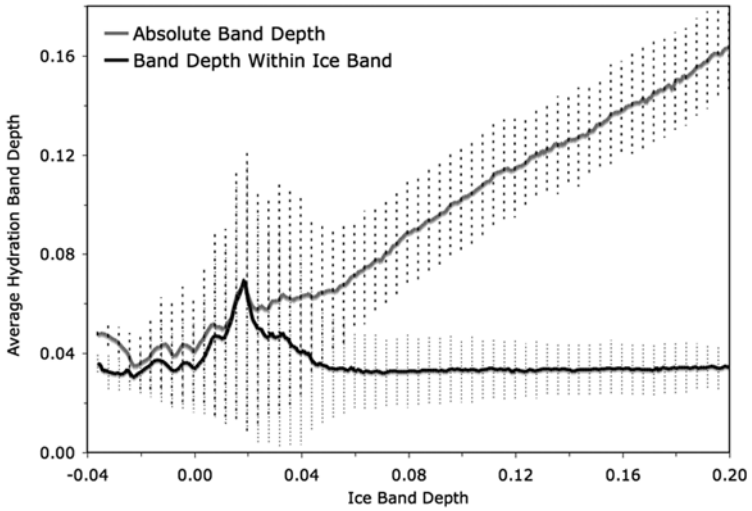

Figure 4. Regionally averaged 1.9 μm hydration band depth for varying 1.5 μm ice band depths.1.9 μm band depths calculated using standard method (gray line) and relative to 2 μm ice band (black line). Error bars are 1 standard deviation. The peak at 0.02 represents the region in Olympia Planum with > 15% 1.9 μm band depths (see Figure 5), as this region also exhibits 1.5 μm ice band depths between 1 and 3%, with smaller ice band depths farther from Planum Boreum.

here exploits the symmetry of the 2 μm water ice band to provide a way to include even ''water ice-contaminated'' surface regions in our analysis.

[45] For spectra that are water ice-rich, we search for the 1.9 μm hydration band by evaluating the percentage depth of the 1.9 μm value below the value of the wavelength on the opposite side of the water ice band, at 2.11 μm, as shown in Figure 3c, and as expressed in equation (2):

$$BD(1.934) = 1 - \frac{CR(1.934)}{CR(2.108)} \tag{2}$$

To compensate for the negative overall slope (and therefore slight asymmetry in the 2 μm water ice band) of the water ice-rich spectra in the presence of darker materials (see Figure 3d), we use continuum-removed spectra for this step, represented as CR(wavelength) in equation (2), where the continuum is defined between 1.84 and 2.2 μm [*Poulet et al.*, 2007]:

$$CR(x) = R(x) \Bigg/ \cdot \left(\left[\frac{R(2.205) - R(1.842)}{2.205 - 1.842} \right] (x - 1.842) + R(1.842) \right) \tag{3}$$

Because the water ice band is fairly symmetric at the spectral resolution of the OMEGA instrument, this gives us a good estimate of the hydration band depth. It must be noted that this method does not work when applied to a pure water ice spectrum, like that shown in Figure 3c, as there is no negative slope imposed across the water ice band without the presence of darker material. However, all Martian spectra that we have examined have, at minimum, some amount of dust contamination, which imposes a slight asymmetry on the water ice band. Thus, we believe that using continuum removed spectra will indeed yield a more accurate 1.9 μm band depth.

[46] We have parameterized the presence of the water ice spectral features by the band depth of the 1.5 μm water ice overtone absorption band. This band depth is determined by evaluating the depth of a spectrum at 1.5 μm below a continuum established at 1.3 and 1.7 μm, as shown below, where we have averaged all 3 points with neighboring wavelengths [*Poulet et al.*, 2007]:

$$BD(1.507) = 1 - R(1.507) \Bigg/ \left(\left(\frac{R(1.707) - R(1.292)}{1.707 - 1.292} \right) \cdot (1.507 - 1.292) + R(1.292) \right) \tag{4}$$

[47] Because the standard method for calculating hydration band depth (equation (1)) [*Clark and Roush*, 1984] works well for water ice-free terrains, we have applied the standard method to spectra with 1.5 μm water ice band depths below 2%. Figure 4 shows the average 1.9 μm hydration band depth for a given 1.5 μm water ice band depth across the north polar region, calculated using both the standard (equation (1)) and new methods (equations (2) and (3)) described above. For the standard method, hydration band depth has a clear correlation with water ice band depth, whereas for hydration band depths found relative to the 2 μm water ice band, the hydration band depth is independent of water ice band depth. Below 2% 1.5 μm water ice band depth, both methods produce similar results, and we can apply the standard method to those spectra; however, it should be noted that the nonstandard approach appears to underestimate the 1.9 μm band depth for spectra with 1.5 μm band depths less than 2%, by about 1%

(see Figure 4). This is caused by the slightly more negative slope of continuua taken between 1.84 and 2.12 μm versus those taken between 1.84 and 2.2 μm. Ideally, in water ice-free materials, these slopes should be identical. The decrease in slope may be due to the presence of the 2 μm water ice band, or the presence of a 2 μm pyroxene band. The major impacts of this discrepancy on our mapping efforts are (1) a discontinuity of < 3% in hydration band depth at some contacts between water ice-free and water ice-rich surfaces, and (2) that by imposing the same detection threshold on the hydration band depth calculated using both methods, we may be losing sensitivity to band depths near that detection threshold in water ice-rich terrains.

[48] As a final measure to ensure that we are not detecting anomalous features within the 2 μm water ice band, such as remnant features from poor corrections of the 2 μm CO_2 atmospheric bands, we require that for spectra to have a positive identification of the 1.9 μm hydration band, their minimum between 1.84 and 2.12 μm must be at 1.94 μm or 1.955 μm. This also guarantees that we are not applying this method to pure water ice spectra, which, when the continuum is removed, would yield a negative 1.9 μm band depth.

4.3. Map Limitations

[49] The presence of steep scarps and deep troughs in Planum Boreum creates several problems for our mapping effort. On extremely steep slopes, high incidence angles cause Sun glints off of the specularly reflecting surfaces, which saturate the pixel and washes out any useful spectral features. As such, we are unable to detect spectral features along the walls of troughs at these unfortunate phase angles. Searching for spectral features within troughs is also problematic because at the incidence angles common in northern summer ($\sim$60–70°), either wall of a trough may be in shadow. To correct for the effects of both of these issues in our maps, we have overlaid multiple observations of the same area and searched for the maximum hydration signature in each pixel. This method also allows us to include observations of the same regions taken throughout the early summer and record the hydration at the minimum amount of frost coverage during that time.

[50] As we are including observations taken during a range of solar longitudes and resolutions, boundaries between images in our maps reflect these variations. Images with better resolutions will tend to exhibit higher band depths, especially in the circumpolar plains, where hydration signature-bearing materials are present in sparse dune fields (Figure 5). Additionally, as the fine grained, seasonal water frost deposits continue to retreat poleward into the early summer ($\sim L_S = 107$) [*Langevin et al.*, 2005b], regions with coverage limited to the very early summer will record the presence of seasonal frost close to Planum Boreum. Examples of seams between images that are apparent owing to these effects are present in our maps near 45, 75, and 270°E.

5. Results

5.1. Hydrated Mineral Distribution

[51] Figure 5 shows our 1.9 μm hydration band depth mapped over the north polar region, calculated using the methods described above. The noise uncertainty of the OMEGA data is approximately 2% [*Bellucci et al.*, 2006]; however, we estimate that our detection threshold in this map is 4.5% band depth. Below this threshold, the hydration signature appears noisy, but above this threshold it begins to show spatially contiguous correlations with geologic features.

[52] The hydration signature is an indicator of the presence of molecular water, either adsorbed onto minerals and/or ice, or bound within the crystal structure of hydrated minerals [e.g., *Clark*, 1981a]. Because the hydration signature exhibits spatially contiguous correlations with geologic features for 1.9 μm band depths above 4.5%, we propose that we are observing hydrated minerals in this band depth regime. As such, we interpret Figure 5 as a map of the distribution of hydrated minerals in the north polar region. It is possible that the noisy signals below 4.5% band depth that we have observed throughout the north polar region may be indicative of the widespread presence of adsorbed water on anhydrous minerals [e.g., *Jouglet et al.*, 2007; *Milliken et al.*, 2007]. Adsorbed water, as identified by the 3 μm hydration feature in OMEGA data [*Jouglet et al.*, 2007], has been observed to increase with latitude poleward of 50°N, and abundances have been estimated at >8 wt % during northern summer [*Milliken et al.*, 2007]. As such, we are unable to differentiate the presence of hydrated minerals from the presence of adsorbed water for 1.9 μm band depths less than $\sim$4.5%.

[53] The maximum hydration band depths that we observe at the resolution of our map (1 km/pixel) are approximately 26%, and are located in the extreme northeastern region of Olympia Planum, near the contact with Planum Boreum. Indeed, the entirety of Olympia Planum exhibits elevated hydration band depths relative to the rest of the region, consistent with the results of *Langevin et al.* [2005a]. In addition, many other areas in the north polar region also exhibit hydration band depths above our threshold, including nearly all of the circumpolar dune fields, the cavi of Planum Boreum, Chasma Boreale, and all of the dark veneers on Planum Boreum. The hydration band depths in these areas are generally below 10%, with a few local exceptions.

[54] The apparent dichotomy in the hydration band depths between Olympia Planum and the other hydrated terrains in the north polar region leads us to speculate that we are observing at least two units containing hydrated minerals: (1) deposits with high concentrations of gypsum [*Langevin et al.*, 2005a; *Fishbaugh et al.*, 2007], restricted geographically to Olympia Planum, and (2) deposits with low concentrations of an unknown hydrated mineral, widely distributed throughout the cavi of Planum Boreum as well as the circumpolar erg. The veneers and circumpolar erg may each represent unique deposits containing hydrated minerals, or the hydration in the erg may be related to that in Olympia Planum.

5.2. Variation of Water Ice Band Depths in Hydrated Terrains

[55] The only major spectral characteristics of the polar regions exhibiting hydration signatures that change significantly across the region are the depths of the 1.5 and 2 μm water ice bands. Figure 6 shows spectra, created from averages taken across the north polar region, that represent spectral units defined in terms of the presence or lack of the 1.9 μm hydration signature and the depth of the 1.5 μm water

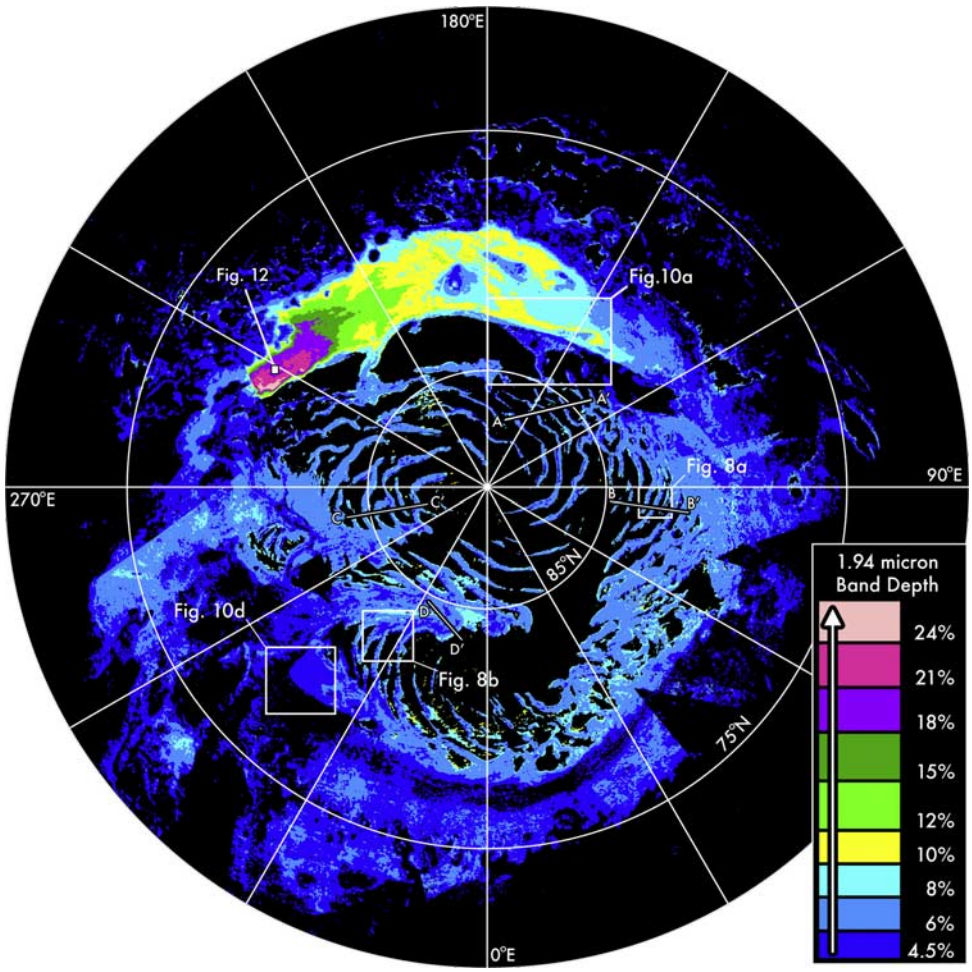

Figure 5. Polar stereographic map of the 1.9 μm hydration band depth in the north polar region. Color contour levels have been chosen to illustrate variation in band depth. Contours indicate band depths greater than 4.5, 6, 8, 10, 15, 18, 21, and 24%, respectively. Insets and profiles indicate locations of Figures 8, 10, and 12.

ice band. These spectra are samples of a continuum of spectra with water ice band depth ranging from 0 to over 60%.

[56] Figure 7 shows these 6 spectral units mapped over the north polar region. Regions bearing hydration signatures in the circumpolar plains are generally water ice-free, and water ice band depth increases with proximity to Planum Boreum. Specifically, we observe water ice-rich hydrated units in the mixed- and low-albedo regions identified as veneers by *Rodriguez et al.* [2007], on the margins of Planum Boreum, on the margins of the icy outliers, and in the narrower polar troughs and reentrants, many of which have been previously identified as containing dark, water ice-free materials [*Tanaka*, 2005; *Tanaka et al.*, 2008; *Rodriguez et al.*, 2007].

[57] *Rodriguez et al.* [2007] proposed, on the basis of OMEGA data, that the mixed- and low- albedo terrains represent linear mixtures of water ice and the overlying dark veneers. Because we also observe hydrated units with water ice bands at contacts between dark water ice-free and bright water ice-rich terrains, these units are also most likely subpixel, spatial mixtures of water ice and dark, hydrated terrain. On the margins of Planum Boreum and at the edges of troughs, the dark materials may be simply abutting water ice-rich surfaces. This conclusion is supported by the preliminary results of *Langevin et al.* [2008], which also suggest an areal mixture between icy terrains and the adjacent PLD surfaces in OMEGA data. Simple linear mixtures of the spectra for unit 1 and ice (water ice) shown in Figure 6 yield approximate fits for units 2–4 for surface water ice abundances of ~10, ~25, and ~50 wt %.

[58] With the exception of the variation of the water ice bands, the spectra of the hydrated regions outside Olympia Planum are fairly homogenous. The variations are largely only in albedo, and have a standard deviation of ±~0.05 estimated Lambert albedo for the hydrated spectral units, as shown in Table 2. The hydration signature is found in dark-toned sand dunes, dark-toned veneers, and dark-toned layered deposits in Planum Boreum, with spectra that are nearly featureless, except for the 1.9 μm hydration band and a broad 1 μm band (see the Unhydrated unit and unit 1 in Figure 6) that may be due to a ferrous component in the dark material. The spectral homogeneity of the dark, hydrated materials is consistent with the idea that the polar layered deposits and the circumpolar erg have exchanged materials in many episodes, throughout the Amazonian.

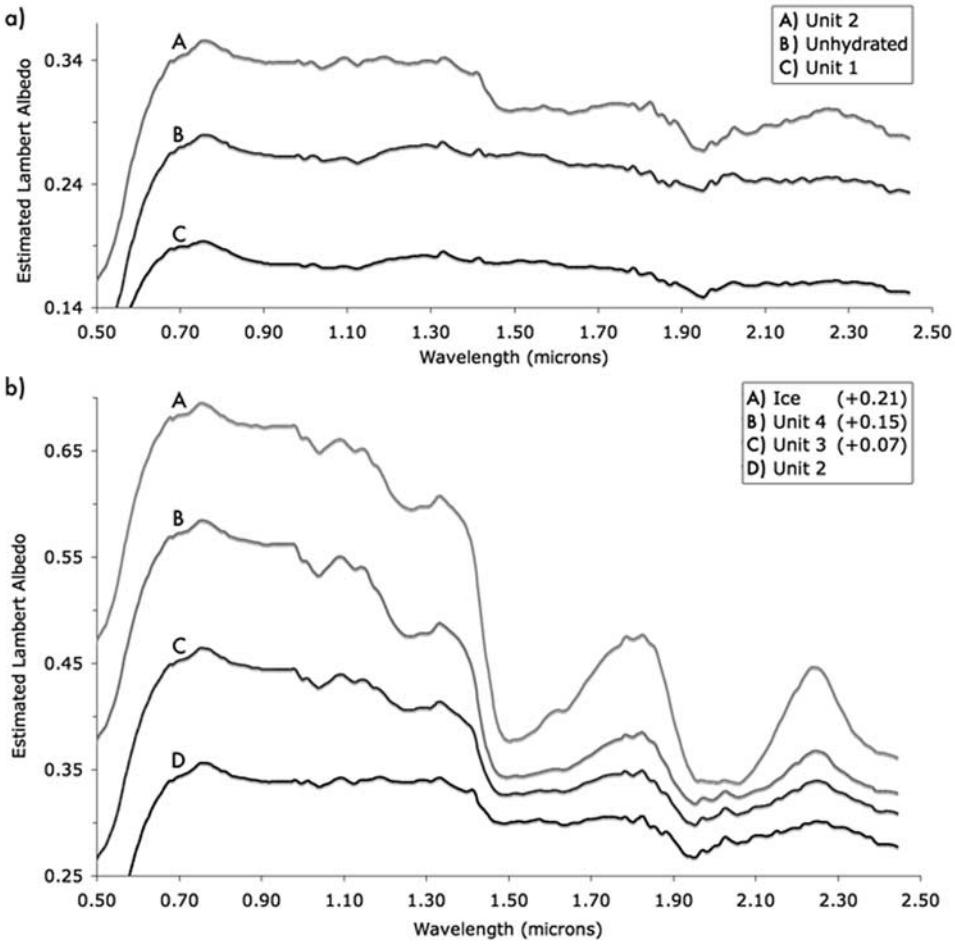

Figure 6. OMEGA spectra with > 4.5% 1.9 μm hydration band depth and with increasing 1.5 μm ice band depths, averaged over the north polar region. The 1.9 and 1.5 μm band depth criteria used for determining spectral types are given in Table 2. (a) Hydrated ice-free, hydrated ice-poor, and unhydrated ice-free units. Unhydrated unit exhibits a minor hydration band due to the inclusion of terrains with 1.9 μm band depths between 0 and 4.5%. (b) Ice-rich hydrated and pure ice units. Spectra have been shifted upward in albedo by the amount indicated in the legend for ease of viewing. Unit 2 is shown in both plots for continuity. Together, these spectra represent a continuum of ice band depths throughout the hydrated terrains that we observe in the north polar region.

5.3. Correlations With Geologic Units

[59] After a comparison of Figures 2 and 7, on the regional scale, the hydrated minerals in Planum Boreum appear to be correlated with the Planum Boreum 1 unit of *Tanaka et al.* [2008]; however, this may not be accurate under closer inspection. Figures 8a and 8b show the hydration signatures associated with troughs near 90°E and 270°E, respectively, alongside the THEMIS albedo and the *Tanaka et al.* [2008] geologic map from the same area. The hydration signature does not cover the entire trough where dark layers are visible and the Planum Boreum 1 unit has been mapped, but rather seems to start 1–3 pixels below the top of the layers. Figures 9a–9d show OMEGA hydration, MOLA elevation, THEMIS albedo, and OMEGA water ice band depth profiles taken through many of the troughs on Planum Boreum. The troughs all exhibit hydration signatures on their equatorward slopes as well as on their floors, and the zone of hydration appears to be sharply defined. On the poleward slope, the sharp drop-off of the hydration signature is accompanied by a sharp increase in the water ice band depth. When compared to similar profiles taken by *Tanaka et al.* [2008, Figure 4b] through the geologic units, it appears that the hydration signature is cut off on the poleward slope by the presence of the Planum Boreum 3 unit.

[60] On the equatorward slope of the troughs shown in Figures 9a–9d, the hydration signature rapidly increases just after the start of the dark layers, as indicated by the decrease of the THEMIS albedo. The hydration signature is consistently greatest at its uppermost extent on the slope, and decreases downslope, possibly indicating a source of hydrated material near the top that is actively eroding and covering/coating lower units. This region of the slopes near the contact of Planum Boreum 1 and 3 units may correspond to the Planum Boreum 2 unit, the thin, dark, sandy unit intermediate between the upper and lower layered deposits, identified by *Rodriguez et al.* [2007].

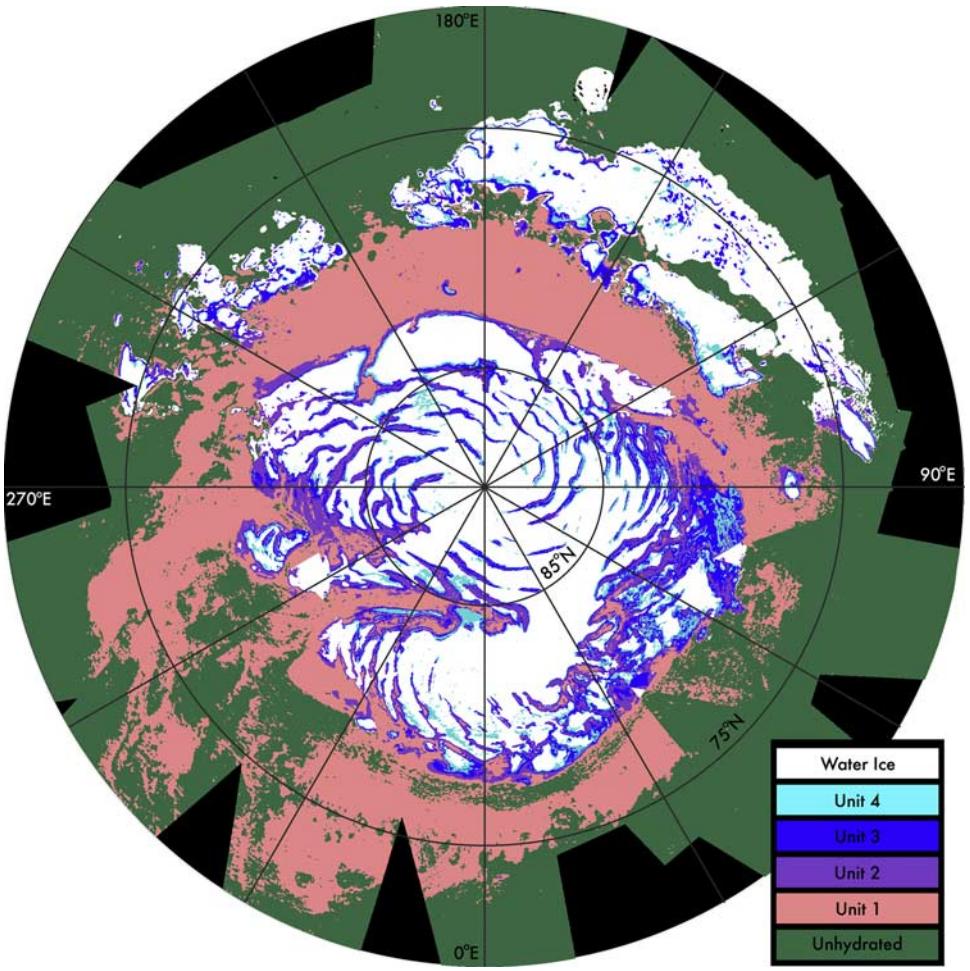

Figure 7. Polar stereographic map of the distribution of OMEGA-derived variations in the 1.5 μm ice band depth within hydrated terrains in the north polar region. Spectral types are defined in Table 2 and shown in Figure 6. Ice band depth increases with proximity to margins of Planum Boreum 3 and 4 units.

[61] As shown in Figures 9a–9d, we have consistently observed this ''gap'' in the hydration signature in the Planum Boreum 3 unit below the tops of troughs at all orientations across the polar cap, which leads us to believe that this is a real feature and not an artifact owing to misregistration. In addition, the hydration signatures at the edges of these gaps consistently rise sharply to significant band depth values, as would be expected if the source of the hydration is a well-defined layer, such as the veneer-forming Planum Boreum 2 unit. If the residual cap was merely obscuring hydration at the top of trough, it is unlikely that we would observe this feature so consistently across the polar cap.

[62] From these observations, we may postulate that the Planum Boreum 3 unit does not contain hydrated minerals, but that the Planum Boreum 2 unit does. If this is the case, then the units stratigraphically below the Planum Boreum 2 unit are likely to be coated in eroded material from this unit, as indicated by the fall-off in hydration band depths within the troughs in Figures 9a–9d. This debris would obscure any inherent hydration signature the underlying units might have, and as such, we cannot comment on their abundance or lack of hydrated minerals. We have noted, however, that the Rupes Tenuis unit, where it is exposed away from the over-

Table 2. Constraints on and Deviation of Our Defined Spectral Units

			Standard Deviation[a]	
Spectral Unit	1.9 μm Band Depth	1.5 μm Band Depth	Average	Median
Unhydrated	<4.5%	<3%	0.064	0.071
Unit 1	>4.5%	<3%	0.058	0.065
Unit 2	>4.5%	3–10%	0.065	0.067
Unit 3	>4.5%	10–20%	0.046	0.043
Unit 4	>4.5%	>20%	0.046	0.040
Ice	<4.5%	>3%	0.085	0.089

[a]Standard deviation units: estimated Lambert albedo. Averages and medians were calculated from standard deviations for each wavelength of the average spectral unit spectra shown in Figure 6.

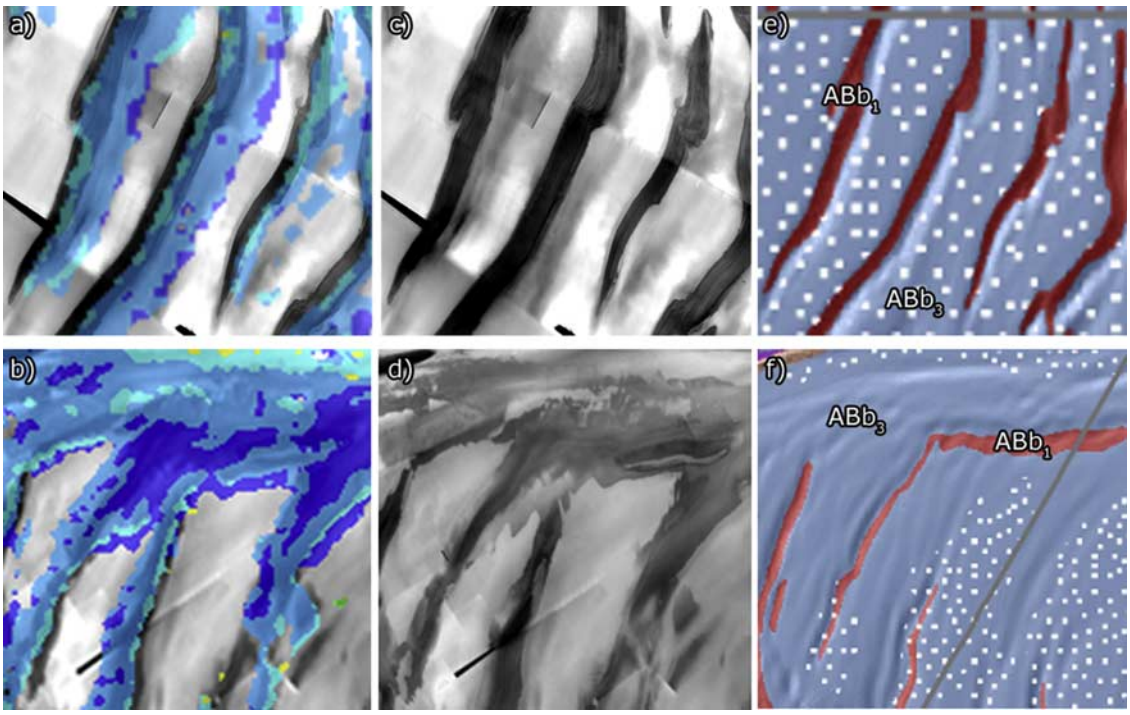

Figure 8. 1.94 μm hydration signatures associated with veneers sourced from units within polar troughs (see Figure 5 for locations). (a) Hydration signatures emanating from troughs near 90°E. (b) Hydration signatures emanating from troughs on the eastern wall of Chasma Boreale. The topmost layers exposed in the troughs do not exhibit hydration at the resolution of our map (at best 1.6 km/pixel); however, all lower layers do. (c and d) Visible images of regions shown in Figures 8a and 8b from 36 m/pixel THEMIS north pole mosaic (N. Gorelick, ASU). The darkest, and presumably youngest, veneers emanating from the troughs also exhibit hydration signatures, while the older, brighter veneers do not. Hydration signatures correlate well with dark veneers, and again, uppermost dark layers exposed in troughs do not exhibit hydration at this scale. (e and f) Segment of *Tanaka et al.* [2008] geologic map. Hydration signatures are present in troughs below Planum Boreum 1 unit (ABb_1). Planum Boreum 2 unit is not mapped at these scales.

lying units, does not exhibit a hydration signature at the resolution of our map.

5.4. Correlations With Sedimentary Veneers

[63] Comparing Figures 1 and 7 reveals that the regions on Planum Boreum that exhibit a hydration signature but are not in troughs have a lower albedo than the surrounding water ice. These areas correspond to the north polar veneers identified by *Rodriguez et al.* [2007]. Figure 8 shows two examples of veneers on Planum Boreum emanating from troughs. In Figure 8a, the hydration signature extends from the trough downslope to the margin of the darkest veneers shown in Figure 8c. In Figure 8b, the hydration signature tracks veneers that have spread both up and downslope from the troughs shown in Figure 8d. While hydration is not detected in all of the veneers evident in Figures 8c and 8d, hydration is detected in all of the darkest, stratigraphically youngest veneers.

[64] *Rodriguez et al.* [2007] interpreted the Planum Boreum 2 unit as the source unit for the veneers emanating from troughs. Our observation that these veneers are hydrated provides further support for the idea that the Planum Boreum 2 unit is the source of the hydrated minerals that we have detected in the troughs and on the surface of Planum Boreum.

[65] Where the veneers are transported off of Planum Boreum, they form mantles around the periphery [*Rodriguez et al.*, 2007]. Several of these mantles embay dune fields, allowing us to observe the contact between these two hydrated sedimentary deposits. Figure 10a shows a veneer mantling the periphery of Planum Boreum and the margin of western Olympia Planum. The bright water ice of the Planum Boreum 3 unit covers and embays many fossilized dunes at its margin, as shown in Figures 10b and 10c. Although the ice is covered with the veneer to its margin, it is unclear how far out the veneer extends past the ice and into the dune field, if at all. Moving off of the ice, the hydration signature increases in the plains with sparse dunes, and increases again at the main margin of the dune field. If the veneer does extend past the ice margin, it may be mixing with hydrated material from Olympia Planum to create a hydration band depth between that of the veneer and that of the main dune field. On the other side of Planum Boreum, Figure 10d shows the Planum Boreum 3 unit and the veneer covering it at the tip of Gemina Lingula. The ice mantles and embays dunes, as shown in Figure 10f [*Rodriguez et al.*, 2007]. Because the veneer embays the dunes, this suggests that the veneer has been more recently mobile than the dunes. The veneer exhibits a

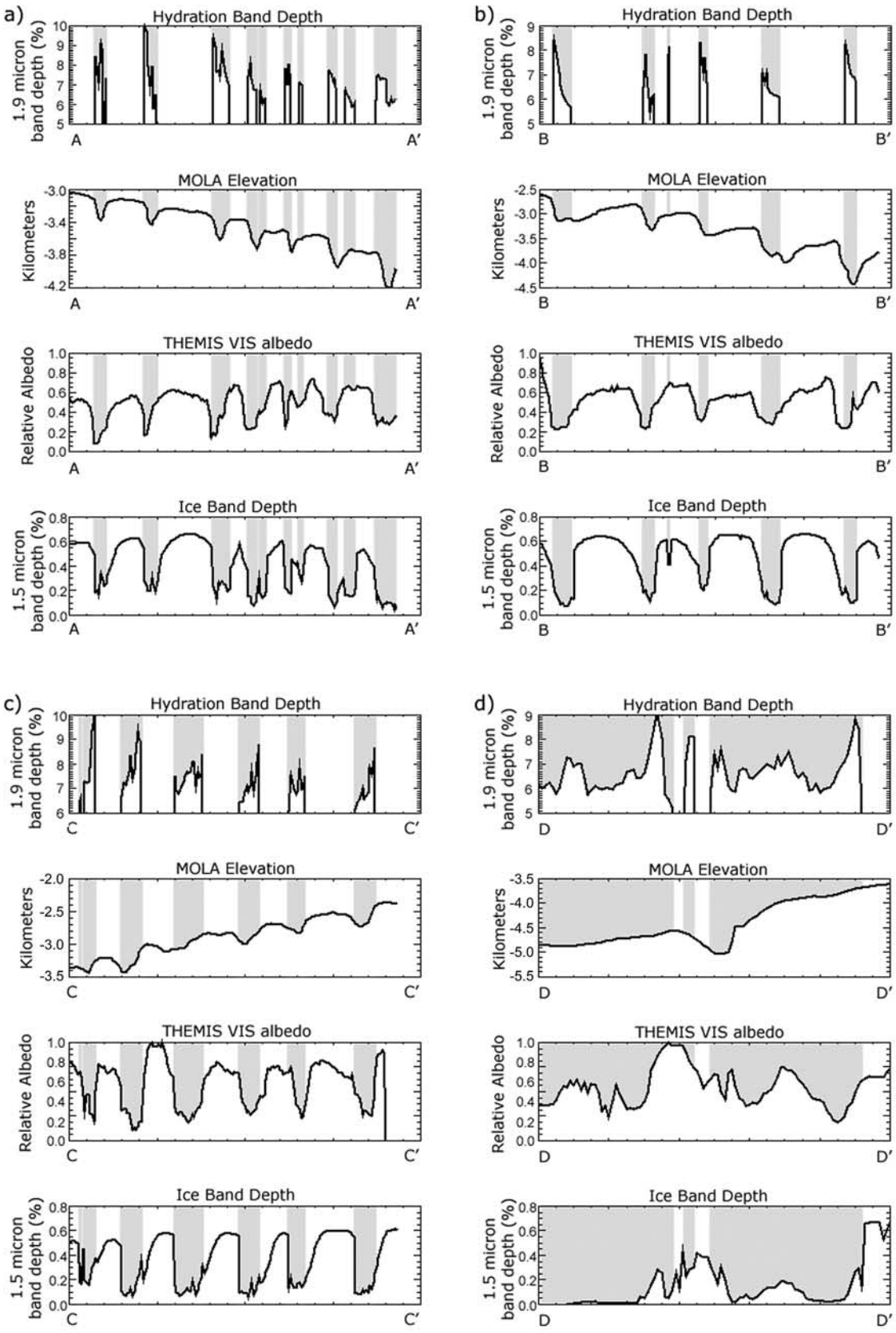
a)
Hydration Band Depth
1.9 micron band depth (%)
A
A′
MOLA Elevation
Kilometers
THEMIS VIS albedo
Relative Albedo
Ice Band Depth
1.5 micron band depth (%)
b)
B
B′
c)
C
C′
d)
D
D′

Figure 9

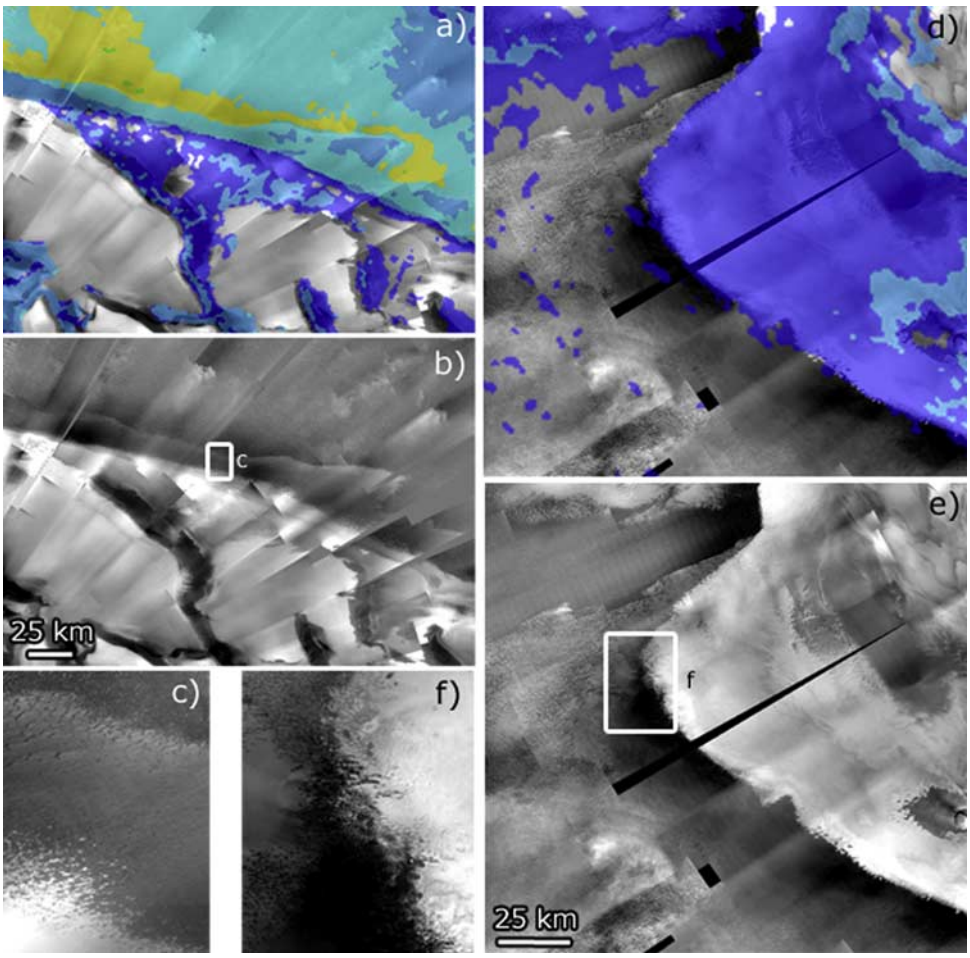

Figure 10. Contacts between hydrated veneers and circumpolar dune fields. Visible images from 36 m/pixel THEMIS north polar mosaic (N. Gorelick, ASU; see Figure 5 for locations, scale, and 1.9 μm band depth color legend). (a and b) Hydrated veneers mantle dunes of the Olympia Planum erg. The 1.94 μm hydration signature of gypsum-bearing Olympia Planum dunes is muted by the veneer to a band depth between those exhibited by the veneer and unmantled dunes, implying that spectral mixing is occurring. The mantling also indicates that the veneer has been mobile and dynamic more recently than the dunes. (c) Close-up of zone of muted dunes, as indicated by the inset in Figure 10b. Because the duneforms, albedos, and hydration signatures are apparent under the mantle, here it must be relatively thin (order several μm). (d and e) Hydrated veneers mantle dunes near the mouth of Chasma Boreale. Dunes are either unhydrated or hydrated at a level below our detection threshold of 4.5% 1.9 μm band depth. (f) Close-up of mantled dunes, as indicated by the inset in Figure 10e. Duneforms are indistinct under mantle, indicating much greater thickness (a fraction of the height of the dunes, order meters).

hydration signature above our threshold, but the dunes do not, which suggests that (1) the veneer does not extend past the ice at this location, and (2) this particular dune field has not been contaminated by hydrated material from Olympia Planum (see section 5.5).

5.5. Correlations With Dune Fields

[66] In the circumpolar plains, the hydration signatures we observe are largely correlated with the presence of dune fields, as mapped by *Tanaka and Hayward* [2008]. In general, the hydration band depth decreases with a decrease

Figure 9. Comparison of colocated profiles of OMEGA 1.94 μm hydration band depth, MOLA elevation, THEMIS albedo, and OMEGA 1.5 μm ice band depth. Profile locations shown in Figure 5. (a) Profiles through troughs near 150°E. (b) Profiles taken through troughs near 90°E. (c) Profiles taken through troughs near 270°E. (d) Profiles taken over the Chasma Boreale head scarp. Grey bands indicate surfaces with hydrated mineral detections. All profiles indicate that hydrated deposits are present throughout the trough cross sections and are associated with dark material and low ice band depths. All profiles also consistently show elevated and sharply truncated hydration signatures on the steep, equatorward scarps of the troughs. This may indicate a source unit for hydrated minerals in the scarps, the erosion of which would spread hydrated minerals at lower abundances throughout the trough cross section and into or onto the veneers between troughs.

in dune areal density, and both of these parameters decrease with distance from Olympia Planum, in the east and southeast directions [*Tanaka and Hayward*, 2008; *Hayward et al.*, 2008]. This suggests that Olympia Planum is the source region for much of the dune material [*Tanaka et al.*, 2008], and also that at least some of the hydrated mineral present in all of the circumpolar dunes is gypsum from Olympia Planum.

[67] In comparing the dune density map of *Tanaka and Hayward* [2008] with Figure 5, it appears that, in general, dune areal density correlates with hydration band depth. Because sparser dune fields offer less total exposed area of hydrated minerals for us to detect at the resolution of our maps, this may imply that the dunes exhibit a fairly uniform abundance of hydrated minerals throughout the circumpolar plains. However, there are disparities between dune density and hydration band depth. For example, the region to the southeast of Chasma Boreale is mapped as containing fairly dense dune fields, but exhibits only scattered hydration band depths above our threshold. This may be a resolution issue in the hydration band depth map, or this may indicate a difference between the dunes forming the circumpolar "ring" and the dunes in this region. These dune fields have been proposed to have been sourced from Chasma Boreale [*Tanaka et al.*, 2008; *Tanaka and Hayward*, 2008], and the lack of widespread hydration signatures may indicate that the source for these dunes contains less hydrated minerals than the dunes sourced from Olympia Planum. It is possible that the mantling of some of the dunes by ice and veneers on the margins of this region (Figure 10d) suggests that these dunes are inactive, and that these dunes may be mantled with another deposit so that any hydration signature they would otherwise exhibit is obscured. However, the putative dune source at Abalos Mensae [*Tanaka*, 2005; *Tanaka et al.*, 2008; *Tanaka and Hayward*, 2008] also exhibits low and subthreshold hydration band depths, indicating that sources outside of Olympia Planum may, in general, contain a significantly lower abundance of hydrated minerals.

[68] Another disparity in the correlation between dune density and hydration can be found in the region between the margin of Planum Boreum and the mapped dune fields, between −30°E and 60°E. While there are no dunes mapped in this region [*Tanaka and Hayward*, 2008], and our subsequent searches with CTX images (e.g., P02_001651_2567_XN_76N006W) have also not revealed any recognizable bed forms, this region is characterized by a low-albedo mantle that may be sourced from the veneers. The separation of the dunes in this region away from Planum Boreum suggests that strong katabatic winds may be the dominant wind regime here [*Tanaka and Hayward*, 2008], which would allow transportation of the veneers off of Planum Boreum. Indeed, it is quite possible that much of the hydration signature in Chasma Boreale and in other areas adjacent to the polar cap may be due to the presence of the veneers (K. Tanaka, personal communication, 2008).

5.6. Spectral Relationships

[69] *Langevin et al.* [2005a] identified the dominant hydrated mineral present in Olympia Planum as gypsum on the basis of the presence of spectral features diagnostic of gypsum at 1.4, 1.75, 1.9, and 2.4 μm. Our results agree with this interpretation in the high 1.9 μm band depth region of Olympia Planum. As shown in Figure 11a, when the dark

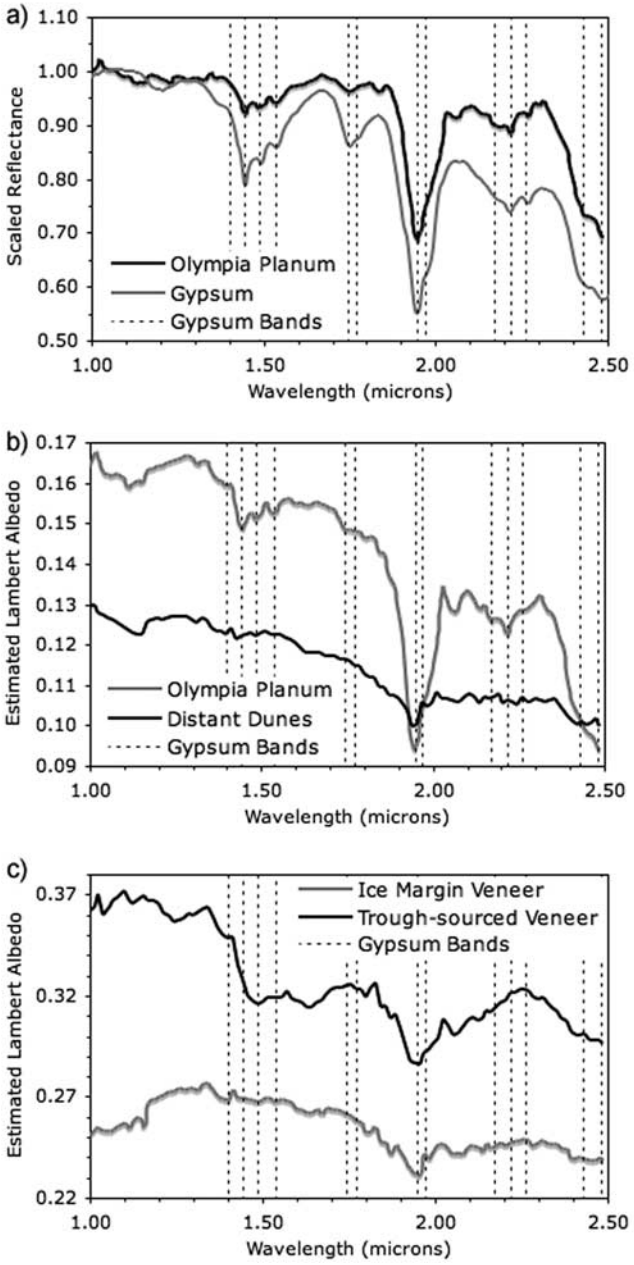

Figure 11. OMEGA spectra of selected localities. In all plots, dotted vertical lines indicate gypsum absorption bands [*Cloutis et al.*, 2006]. (a) Black line is the ratio of Olympia Planum hydrated mineral-bearing terrain (~10 km^2 average; 80.0°N, 245.2°E) and similar albedo terrain with subthreshold (~3%) 1.9 μm band depth (~20 km^2 average; 81.1°N, 277.4°E). Gray line is the laboratory spectrum of gypsum (<45 μm grain size; SPT127) [*Cloutis et al.*, 2006] scaled for similar 1.9 μm band depth. Both spectra have been scaled to 1 at 1.01 μm. (b) Spectral comparison of Olympia Planum gypsum-rich dunes (~10 km^2 average; 80.0°N, 245.2°E) and hydrated mineral-bearing dunes 85° longitude distant (~10 km^2 average; 73.6°N, 330.8°E). (c) Spectral comparison of veneers sourced from Planum Boreum troughs (~4 km^2 average; 82.4°N, 70.6°E) and veneers at the margin of Planum Boreum (~100 km^2 average; 79.5°N, 316.3°E).

component of the dunes is approximately removed by dividing by the spectrum of a similar albedo area with negligible hydration (< 3% 1.9 μm band depth), the remaining spectrum matches well with a laboratory spectrum of gypsum. Unfortunately, because the reference spectrum does exhibit minor amounts of hydration (albeit below our detection threshold), this method does not produce such clear results in the terrains outside of Olympia Planum, which exhibit < 10% 1.9 μm band depth. Alternatively, visual comparison of the OMEGA spectra from various regions to the spectrum of the gypsum-rich dunes does provide some insight. Figure 11b shows a comparison between the spectra of gypsum-rich dunes and dunes 85°E of Olympia Planum. While we cannot make a clear identification of the presence of gypsum in the distant dunes, their spectrum does appear to exhibit a 2.4 μm shoulder and may exhibit a 1.4 μm band, which together, are diagnostic of polyhydrated sulfates [*Cloutis et al.*, 2006; *Gendrin et al.*, 2005]. Figure 11c shows spectra of two hydrated Planum Boreum veneers. The top spectrum was selected from veneers directly adjacent to and presumably sourced from a trough near 70°E, and exhibits water ice bands at 1.25, 1.5, and 2.0 μm. The bottom spectrum was selected from veneers near the southwest margin of Gemina Lingula, and appears to be water ice free. Again, while we cannot make a clear identification of gypsum in these spectra, both top and bottom spectra may exhibit a 1.4 μm band, and while a 2.4 μm shoulder cannot be distinguished from the 2.5 μm water ice band in the top spectrum, a 2.4 μm shoulder may be present in the water ice-free, bottom spectrum. In all of these cases, while we cannot make a clear identification of the hydrated component, the spectra are consistent with a polyhydrated sulfate, and it is certainly plausible that gypsum is the dominant hydrated mineral in these deposits.

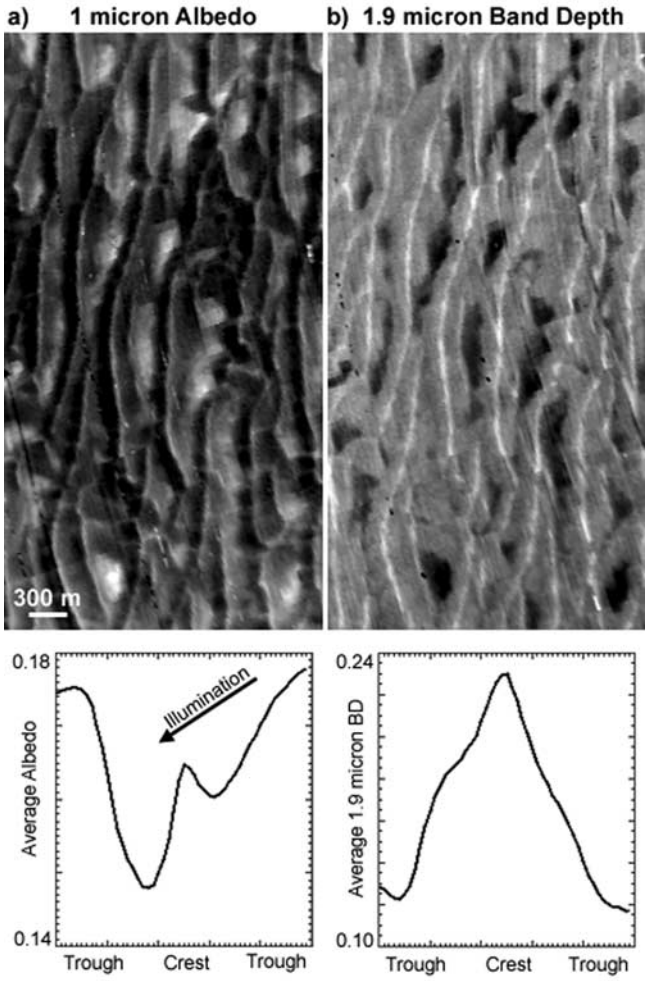

Figure 12. CRISM view of eastern Olympia Planum, near 80.1°N, 240.8°E (CRISM observation FRT0000285f_07; adapted from *Roach et al.* [2007]). Corresponding plots below show average dune profiles calculated from 12 E–W crest-trough profiles and 12 E–W trough-crest profiles throughout CRISM image. (a) 0.95–1.05 μm average CRISM albedo. Dune troughs and crests are both brighter than dune flanks. Asymmetric brightening of right slope in dune profile is due to solar illumination; left slope is in shadow. (b) 1.9 μm band depth. Dune crests have greatest hydration signature (~24%), while albedo bright areas in troughs have lowest (~12%). Brightening of dune crest may be due to gypsum presence.

6. Insights From Laboratory Data Applied to OMEGA and CRISM Observations

6.1. CRISM Observations

[70] Higher-resolution (>18 m) CRISM imagery has provided a greater understanding of how the gypsum is distributed in eastern Olympia Planum, at the scale of individual dunes [*Roach et al.*, 2007]. As shown in Figure 12b, the 1.9 μm band depth, calculated using the method described in section 4.1, has a distinct correlation with dune crests [*Roach et al.*, 2007]. The crests exhibit band depths, on average, of ~25%, as compared to the bright troughs, which exhibit band depths, on average, of ~12%. While this may be due to an increased abundance of gypsum, this is not the only possible explanation. Because increasing grain size also increases band depths, the higher 1.9 μm band depths at the crests have been suggested to be at least partially due to the greater presence of large gypsum grains, as small grains may have been preferentially removed at the crest by the greater wind exposure [*Fishbaugh et al.*, 2007; *Roach et al.*, 2007].

[71] Interestingly, the dune crests also exhibit a higher albedo than the flanks of the dunes, as shown in Figure 12a. Although the rise in albedo on the illuminated side of the dune is due to photometric effects, the rise in albedo near the crest is most likely not, as it is symmetric across both the illuminated and shadowed sides of the dune. This higher albedo at the dune crests does not support the hypothesis that the greater 1.9 μm band depths observed at the crests are due to larger grains, as increasing grain size tends to decrease albedo, as shown in Figure 13a. In addition, in situ terrestrial observations have generally found upslope fining of dune sand, with coarse grains found at the crest only in rare cases due to complications from dune topography and the size distribution of the source [*Finkel*, 1959; *Hastenrath*, 1967; *Vincent*, 1984; *Watson*, 1986]. On the basis of these observations and the fact that gypsum is a light-toned mineral, we suggest that both the rise in albedo and the rise in the 1.9 μm band depth near the crest may be due to the presence of higher abundances of gypsum.

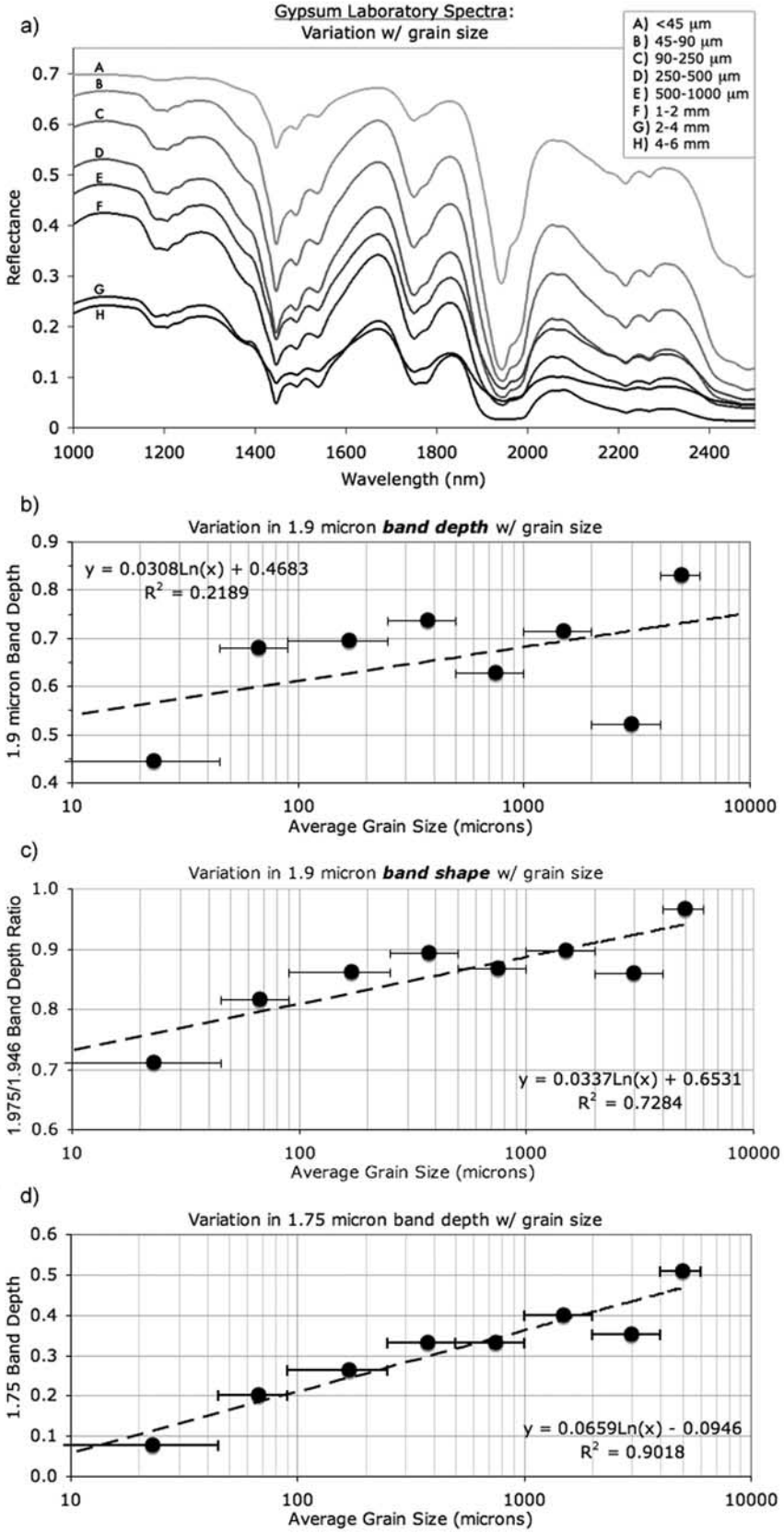
a)
Gypsum Laboratory Spectra:
Variation w/ grain size
A) <45 μm
B) 45-90 μm
C) 90-250 μm
D) 250-500 μm
E) 500-1000 μm
F) 1-2 mm
G) 2-4 mm
H) 4-6 mm
Reflectance
Wavelength (nm)
b)
Variation in 1.9 micron band depth w/ grain size
y = 0.0308Ln(x) + 0.4683
R2 = 0.2189
1.9 micron Band Depth
Average Grain Size (microns)
c)
Variation in 1.9 micron band shape w/ grain size
y = 0.0337Ln(x) + 0.6531
R2 = 0.7284
1.975/1.946 Band Depth Ratio
Average Grain Size (microns)
d)
Variation in 1.75 micron band depth w/ grain size
y = 0.0659Ln(x) - 0.0946
R2 = 0.9018
1.75 Band Depth
Average Grain Size (microns)

Figure 13

6.2. Variation of 1.9 μm Band Depth With Grain Size

[72] While we hypothesize that the increase in 1.9 μm band depth that we have observed between dune troughs and crests in the CRISM observation presented in Figure 12b is due to an increase in gypsum abundance, the possibility that the increase in band depth is due to a change in grain size begs the question: what magnitude of grain size change would be required to increase the 1.9 μm band depth from 12% to 25%? While laboratory studies have been conducted on the optical constants of gypsum [*Roush et al.*, 2007], the spectral properties of gypsum [*Cloutis et al.*, 2006], and the stability of gypsum under Mars-like conditions [*Cloutis et al.*, 2007], empirical models for the changes in the spectral properties with changes in grain size and abundance have not been fully examined. *Ghrefat et al.* [2007] present grain size, band depth relations for sand gathered at White Sands, but only for the 1.75 and 2.15 μm gypsum bands. *Clark et al.* [2008] also present some preliminary findings in this area. To address this deficiency in the literature, here we present our own independent findings on these spectral variations.

[73] Figure 13a shows the laboratory spectra of gypsum samples, dry sieved to various grain size ranges. Reflectance spectra over the 0.35–2.5 μm range were acquired with an Analytical Spectral Devices FieldSpec Pro HR® spectrophotometer. The spectral resolution of the instrument varies between 2 and 7 nm and spectral sampling is done at 1.4 nm intervals. The instrument internally resamples the spectra to 1 nm intervals [*Cloutis et al.*, 2007]. The primary change that occurs with increasing grain size is a widening and deepening of the bands. In addition, the 1.75 and 1.9 μm bands appear to saturate. While our study only sampled grain sizes below 45 μm in one bin, *Cooper and Mustard* [1999] analyzed laboratory samples of montmorillonite for variations in hydration band depths with particle size, and found that small particles (<5 μm) still have detectable (more than several % band depth) 1.9 μm bands.

[74] Figure 13b shows the measured change in 1.9 μm band depth with grain size on a logarithmic scale, calculated using equation (1). While the trendline shown is not a good fit for all the data points (both because we are sampling a range of grain sizes with each spectrum and because of the difficulty in measuring accurate bands near saturation) it illustrates that while this is a complex relationship, there is some dependence on grain size, although poorly defined for this data set. Keeping this in mind, we can extract the general trend from the fit, which is on the order of 5% increase in band depth per order of magnitude change in grain size. If we apply this trend to the CRISM 1.9 μm band depths observed in the gypsum-rich dunes, the grain sizes in the crests would need to be over 100 times greater than those in the troughs for the abundance to remain the same: for example, 1 mm grains in the crests of the dunes would imply ~10 μm grains in the troughs. This scenario is plausible, as extremely fine gypsum grains could be produced by breakdown of larger gypsum grains during saltation.

[75] This change in grain size, if it is real, may be detectable via other spectral analysis methods. A possible method for detecting changes in grain size in gypsum deposits, and possibly other H_2O-bearing mineral deposits, involves analyzing the shape of the spectrum within the 1.9 μm band. The 1.9 μm band is actually a doublet, with centers at 1.94 and 1.97 μm [*Cloutis et al.*, 2006]. As shown in Figure 13a, with an increasing grain size, the minima of the two bands approach the same reflectance value. This is most likely due to the deeper 1.94 μm band saturating first. Figure 13c shows how the ratio between the 1.94 and 1.97 μm band depths changes with grain size: the ratio increases ~18% with an order of magnitude increase in grain size. Ideally, we would like to apply this analysis to CRISM spectra of the gypsum-rich dunes to test for large variations in grain size between the crest and troughs. For the change in grain size required to maintain a constant abundance, the ratio difference between the crests and troughs should be ~40%. Unfortunately, taking the ratio of these band depths enhances what appear to be calibration or low signal-to-noise ratio errors between columns in the CRISM image, obscuring the interpretation of the band depth ratio. Perhaps this method may be applied to CRISM data in the future with an improved calibration routine or with higher signal-to-noise ratio data.

[76] The 1.75 μm gypsum absorption band may also be used to track grain size changes, as demonstrated by *Ghrefat et al.* [2007] at the White Sands dune field. Figure 13d shows the variation of the 1.75 μm band with grain size in our laboratory spectra, calculated using equation (1), with shoulders at 1.680 and 1.825 μm and a band minimum at 1.750 μm. The 1.75 μm band depth appears to correlate well with grain size, without the fluctuations that are apparent with the 1.9 μm band depth (Figure 13a). The 1.75 μm band depth changes ~7% with an order of magnitude change in grain size, and ideally, we should be able to apply this function to the CRISM data. Unfortunately, while the CRISM spectra show 1.75 μm band depths that also are a maximum at the dune crests, the range of 1.75 μm band depths across the dunes is between 0 and 2.5%, which is too small of a change to consider with this method.

[77] While these new methods of constraining grain size have not yielded highly constrained results in this case study, they could prove quite useful in future efforts with a more precise calibration of the CRISM data. For example, with additional CRISM data over Olympia Undae, a future study could use the grain size discrimination methods we have presented to better classify the distribution of gypsum in the dunes, both within the putative source region and in the rest of Olympia Undae. Along with observations of how the dune

Figure 13. Laboratory measurements of variation of gypsum spectra with grain size. (a) Gypsum laboratory spectra. Samples of naturally occurring gypsum (SPT127) [*Cloutis et al.*, 2006] were crushed and dry sieved into the following grain size bins: <45 μm, 45–90 μm, 90–250 μm, 250–500 μm, 0.5–1 mm, 1–2 mm, 2–4 mm, and 4–6 mm. (b) The variation in 1.9 μm band depth with grain size, with a logarithmic fit ($R^2 = 0.2189$). (c) The variation in the shape of 1.9 μm band with grain size, as determined from the ratio of the 1.975 and 1.946 μm band depths, with a logarithmic fit ($R^2 = 0.7284$). (d) The variation in 1.75 μm band depth with grain size, with a logarithmic fit ($R^2 = 0.9018$). Below 500 μm grain size, our data match well with those of *Ghrefat et al.* [2007].

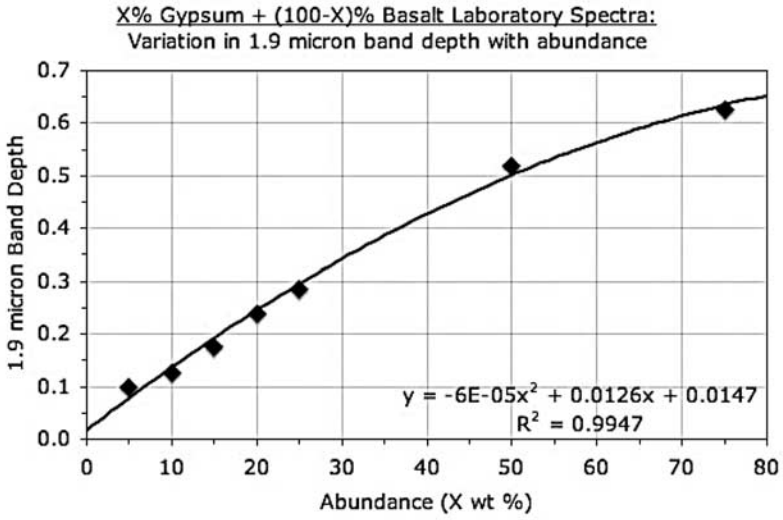

Figure 14. Laboratory measurements of variation of 1.9 μm band depth with gypsum abundance for sand-sized (90–250 μm) mixtures of gypsum and basalt. The trendline shown is a second- order polynomial fit (R^2 = 0.9947) and indicates that the band approaches saturation for abundances greater than ~70 wt %.

profile albedo changes throughout Olympia Undae, these results could give valuable insight into how the gypsum is transported by and deposited on the dunes.

[78] Such a study would also provide great insight into how the distribution of gypsum grain sizes in the north polar erg differs from what we would expect from terrestrial results. Dune fields on other planets are subject to different environments and different gravitational forces. In particular, the gypsum in the Martian north polar erg is a special case because it is a much softer material than the quartz sands that have been studied on Earth. So, when we take into account the vast distances that the gypsum is being transported over in the north polar erg and the order of magnitude higher impact velocities it must experience on Mars than it would on the Earth, it is unclear with how much confidence terrestrial results can be applied to this special case. As such, spectral data on the grain size distribution of the gypsum could provide much needed insight into Martian dune dynamics.

6.3. Variation of 1.9 μm Band Depth With Abundance

[79] Laboratory spectral data have also allowed us to empirically explore how the gypsum 1.9 μm band depth varies with abundance. The relationship between band depth and abundance may potentially be quite complicated; however, for the case of the circumpolar erg, the relationship can be slightly simplified. Because the process of saltation only occurs for a specific distribution of grain sizes [e.g., *Bagnold*, 1941], we can make the assumption that we know the typical grain size in the dunes. Observations from the Mars Exploration Rovers (MER) of basalt sand in recently active aeolian bed forms have indicated grain sizes of 100–300 μm [*Sullivan et al.*, 2008]. For our purposes, we have used a grain size bin with a range of 90–250 μm. To create model mixtures of potential dune components, we created intimate mixtures of basalt and gypsum, with gypsum abundances of 5, 10, 15, 20, 25, 50, and 75 wt %. We have chosen to use basalt because the mafic signatures observed by HST [*Bell et al.*, 1997] and OMEGA (Figure 6) may indicate a similar composition to the sand observed at the MER landing sites and on the rest of the planet [e.g., *Bell et al.*, 2004; *Bibring et al.*, 2005; *Christensen et al.*, 2000, 2004b; *Gellert et al.*, 2004; *Morris et al.*, 2006].

[80] Figure 14 shows the change in 1.9 μm band depth with abundance for the basalt-gypsum sand mixtures, with a second-order polynomial trendline (R^2 = 0.9947). As would be expected, the band depth begins to saturate with high abundances (>70%). We find that sand-sized gypsum should be detectable (above 2–3% band depth) for more than 1–2 wt %. For comparison, *Poulet et al.* [2007] presented a simulated mixture of gypsum and dust, and found that for 5 and 10 μm grains, the detection level of 2% was reached for >10 wt % and >5 wt % abundances, respectively. This indicates that the detection limit decreases with increasing grain size, so our detection limit of 1–2 wt % for sand-sized particles seems to fit into this model.

[81] On the basis of this laboratory data set, and the substantial assumptions that the hydrated minerals are all gypsum grains of sand size (100–300 μm) [*Sullivan et al.*, 2008], that these grains are mixed intimately with materials with spectral properties similar to basalt sand grains, and that the gypsum abundance can be calculated purely from the 1.9 μm band depth, we can make rough estimates for the abundances of hydrated minerals throughout the north polar region. Our threshold 1.9 μm band depth value of 4.5% corresponds to ~7 wt % gypsum, and the hydration signatures outside of Olympia Planum, between 4.5 and 10% band depth, correspond to between ~7 and 13 wt %. The maximum OMEGA 1.9 μm band depth values we observe in eastern Olympia Planum are near 26%, which corresponds to ~30 wt % gypsum. Because both the resolution of our map and the original data are at a scale larger than the dune crest separation distance (0.2–1 km) [*Lancaster and Greeley*, 1990], the spectra we have analyzed represent an areal mixture of the dunes and the troughs. Thirty wt % therefore

corresponds to the "bulk" value for all surface materials at these locations. The band depths we observe in CRISM spectra, as shown in Figure 12b, are typically ~25% at the dune crests, and decreasing down the flanks to ~10% in the bright troughs, which corresponds to a change in abundance from ~30 to ~13 wt % in our model. The maximum band depths we observe in CRISM spectra are ~40%, which corresponds to ~42 wt % gypsum in this model.

[82] Our result of ~30 wt % gypsum determined from OMEGA spectra of the gypsum rich region is somewhat lower than that predicted by the model of *Fishbaugh et al.* [2007], which yielded estimates of 45 wt % 100 μm–1 mm gypsum grains for an intimate mixture with a dark, spectrally featureless material with grains< 45 μm, and nearly 100 wt % gypsum of varying grains sizes for a mixture with inclusions of dark oxide grains. While the 45 wt % gypsum result of *Fishbaugh et al.* [2007] is geologically and spectrally reasonable, the 100 wt % gypsum result, which implies in situ alteration of the dune material, does not seem reasonable in the context of our hypothesis for a sulfate deposit that is older than the dunes.

[83] However, the abundances we have calculated from our model are realistic only if the hydrated phase is indeed gypsum. While we have made the case that it is plausible that the hydrated mineral is gypsum (section 5.5), these results should also be useful if the hydrated mineral is another polyhydrated sulfate. It seems reasonable to assume that the abundance calculated in our model from a given 1.9 μm band depth inherently depends on the number of water molecules in a hydrated mineral; thus, for a mineral with more water molecules per unit cell, our calculated abundance of that mineral (for a given 1.9 μm band depth) must decrease. As such, our estimated abundance of gypsum (2 water molecules per unit cell) will most likely be greater than any other more hydrated sulfate. Therefore, we believe that our calculations also provide a maximum estimate of the abundance of polyhydrated sulfate in the north polar sand sea.

7. Discussion

[84] The distribution of hydrated minerals that we have mapped in the north polar region and its correlations with geologic features and units has raised many questions about the history of the north polar region, both in terms of aeolian transport and water activity. In this section, we discuss the implications of our findings on our understanding of these processes.

7.1. Sources and Transport of Hydrated Minerals

[85] One of the most useful ways our map of the distribution of hydrated minerals in the north polar region can be used is to shed light on the sources and transport pathways of aeolian materials. Our results indicate that most of the circumpolar erg is sourced from the gypsum-rich sands of Olympia Planum, but that the lower hydration band depths of many dune fields in the region near Abalos Mensae and Chasma Boreale indicates that they are primarily sourced from outside of Olympia Planum, presumably from Planum Boreum units exposed in these regions. This may imply that the proposed source units for the dunes, primarily the Planum Boreum cavi unit with some contribution from the Rupes Tenuis unit [*Tanaka et al.*, 2008; *Tanaka and Hayward*, 2008], do not contain hydrated minerals.

[86] The hydrated veneers on Planum Boreum appear to be sourced primarily from the Planum Boreum 2 unit on the basis the work of *Rodriguez et al.* [2007] and the gap discussed above between the hydrated layers and the top of the layered deposits, but an additional source for hydrated minerals in the Planum Boreum 1 unit cannot be ruled out. Given that these veneers may be highly mobile and more recently active than the dunes, the question of how these deposits have interacted still remains. If the veneers are formed from partly sand-sized material, they may contribute to dune formation and/or hydration, either presently or in the past.

[87] The veneer-forming material may have been sourced from Olympia Planum in the Middle Amazonian. If the gypsum in Olympia Planum is sourced from a unit underlying the eastern dune field, it is possible that the epoch of net erosion that carved the polar troughs before the emplacement of the Planum Boreum 2 unit also caused excavation, aeolian or otherwise, of the gypsum deposit, and redistribution throughout the region. After deposition onto Planum Boreum, the gypsum-rich material could have been covered and protected by Planum Boreum 3 and 4 units to this day, when it is now being eroded out of the troughs. This situation illustrates what may have been, and still is, a complex relationship between the units of Olympia Planum and the units of Planum Boreum.

[88] If the hydrated component of the veneer-forming material is not sourced from the Olympia Planum gypsum deposit, then formation of the hydrated component is somewhat of a mystery. Materials on the surface of the topographically elevated and icy surface of Planum Boreum could have been altered by water to a hydrated mineral owing to acidic snow [e.g., *Langevin et al.*, 2005a], but otherwise, the hydrated component must have been sourced from some other, unknown region in the north polar basin.

[89] The presence of a mobile layer overlying an icy core in the dunes, as suggested by Neutron Spectrometer modeling [*Feldman et al.*, 2008], may have implications for the age and dynamics of the dune fields. In particular, it is possible that the putative indurated, potentially icy interiors or cores of the dunes were formed before the gypsum was exhumed from Olympia Planum. In this case, the cores would be free of hydrated minerals, and just the mobile top layer would be enriched. This may explain why not all dune fields exhibit hydration signatures: many of the mantled or indurated appearing dunes may just be the cores of previously active dunes that are not currently participating in aeolian activity. In this case, the hydration signature may indicate more recent aeolian deposition on these dunes, possibly due to the presence of a "mobile layer," as postulated by *Feldman et al.* [2008]. This mobile layer could be partly composed of veneer material. If the identification of a mobile layer is indeed key to understanding the transport pathways of the north polar region, future work on mapping of induration features throughout the circumpolar erg may help reveal its presence and distribution.

7.2. Interpretations of CRISM and HiRISE Data

[90] Our hypothesis of high gypsum concentrations at the crest of dunes in CRISM images raises several questions as to

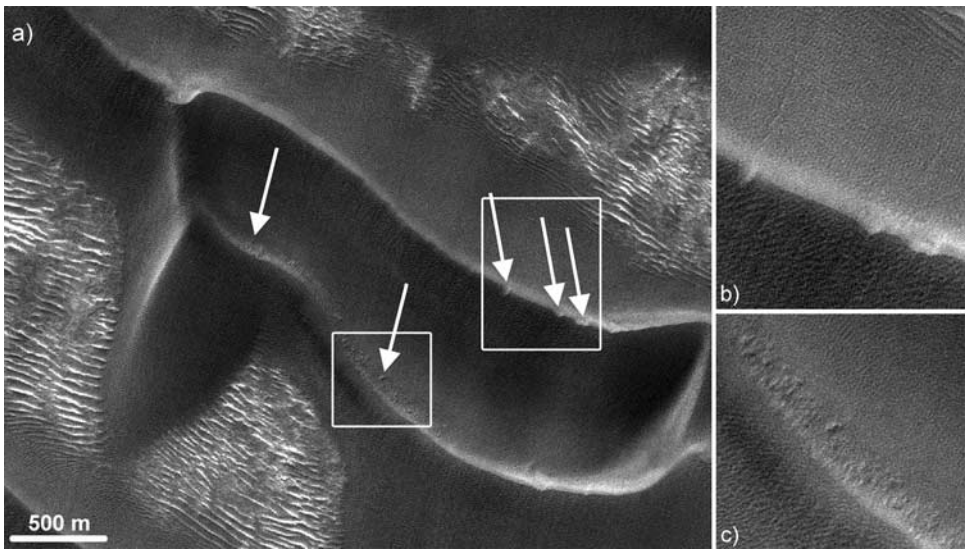

Figure 15. Figure 15a shows a portion of HiRISE image PSP_001457_2600, located near 80°N, 246°E. Dune crests show evidence for induration, in the form of pits and striations, as indicated by arrows and as shown in Figures 15b and 15c. Troughs exhibit transverse aeolian ridges.

the nature of the gypsum within the dunes. Because gypsum is such a soft mineral, loose gypsum grains may be more likely to be broken down at the crest of dunes, where the wind exposure is greatest. Instead, the presence of gypsum at the crest suggests an indurated layer that is preferentially exposed, possibly by erosion of the indurated dune. Figure 15 shows a section of a HiRISE image over the highest gypsum concentration area. The crests of the dune exhibit pits and striations that may indicate induration [*Feldman et al.*, 2008]. Note that the flanks of the dunes do not exhibit similar features indicative of induration. This may support the idea of an indurated gypsum layer exposed only at the crest. Interestingly, neither the crests nor troughs exhibit clear water ice spectral signatures (<3% and <2% 1.5 μm water ice band depths, respectively), which raises the question of how the putative indurated gypsum layer is related to the putative water ice core suggested by Neutron Spectrometer data.

[91] Figure 15 also shows the presence of transverse aeolian ridges (TARs) in the bright troughs. Mars Exploration Rover Sprit observations in Gusev Crater have been used to interpret TARs as coarse grained (several millimeters) granule ripples [*Sullivan et al.*, 2008]. This implies that there should not be a great increase in overall grain size from trough to crest, and assuming that the gypsum size distribution follows that of the dune and ripple forming materials, this further suggests that the observed band depth changes from crest to trough may be indicative of abundance changes. Taking a potential increase in gypsum abundance into consideration with the problems of preserving loose gypsum at dune crests discussed above, this may support our hypothesis of an indurated layer of gypsum.

7.3. Possible Hydrated Mineralogies

[92] While it is possible that all of the hydrated minerals we observe in the north polar region are gypsum, the soft nature of gypsum should make it difficult to keep the grains intact when saltating across large distances, and this puts into question the presence of gypsum in the dune fields farthest away from Olympia Planum (e.g., near 0°E). While we have suggested that the hydrated mineral is most likely a polyhydrated sulfate (section 5.5), we cannot discount other possibilities. For example, the hydration signatures we observe in the dune fields outside of Olympia Planum may be due to another hydrated mineral present at low concentrations in all dune sands sourced from Olympia Planum. This other mineral may be another sulfate, for example, jarosite, which has been identified by the Mars Exploration Rover Opportunity at Meridiani Planum as an aqueous alteration product of mafic materials [e.g., *Morris and Klingelhöfer*, 2008], or some other hydrated phase like ferrihydrite, a nanophase weathering product of basalt [*Deer et al.*, 1992; *Bishop et al.*, 1993; *Jambor and Dutrizac*, 1998]. Future CRISM observations of the hydrated veneers and circumpolar dunes should prove helpful in determining their hydrated mineralogy.

7.4. Implications for Proposed Deposition Mechanisms

[93] If the hydrated minerals in Planum Boreum were indeed sourced from the gypsum deposit in Olympia Planum in the Middle Amazonian or earlier, their existence may not be consistent with the idea that the Olympia Planum gypsum was formed recently owing to interactions between polar outflows and the dunes [*Fishbaugh et al.*, 2007]. However, as Olympia Planum appears to have a long history of dune activity and the underlying materials in Olympia Planum may be the remnants of paleoergs [*Tanaka et al.*, 2008], formation of gypsum in mafic dunes is certainly a plausible formation mechanism farther in the past. Formation in the subsurface due to interactions with acidic groundwater is also certainly still plausible. An additional mode of formation might be deposition of gypsum elsewhere and fluvial transport to the current location, potentially during a catastrophic outflow from the southern highlands.

[94] The fact that high concentrations of gypsum have been observed within a well-defined region of Olympia Planum suggests that this gypsum is being sourced from a coherent, localized deposit. Such a deposit would be unlikely to

accumulate owing to aeolian transportation from outside the region, as aeolian transport would most likely spread such material more uniformly over the north polar region. Therefore, we conclude that this deposit was either formed in situ, or was transported by fluvial processes to its current location. Because the units the gypsum is apparently being sourced from have been identified as having an Amazonian crater retention age and all surrounding units in the region have also been identified as having an Amazonian crater retention age [e.g., *Tanaka et al.*, 2008], we must conclude that the gypsum was either transported to its current location or formed in situ during the Amazonian, either of which require significant water activity in the northern basin during the Amazonian. This conclusion does not fit into the current paradigm of a cold, arid Amazonian [e.g., *Bibring et al.*, 2006]. While the putative water event may have been a one-time, outlier event, it has introduced large quantities of otherwise absent minerals into the north polar region. At minimum, this suggests that singular, landscape altering events may have continued to shape the surface of Mars well into the Amazonian and possibly still are today. At the other extreme, if the proposed water activity was not a singular event in the north polar region, and instead the hydrated minerals represent long-term alteration of surface or subsurface materials, then we must seriously rethink how the current paradigm for the history of water on Mars should be applied to the north polar region.

8. Conclusions

[95] We have generated new maps that enhance our understanding of the distribution of hydrated minerals throughout the north polar region of Mars. These maps provide new constraints on the erosional, transport, and depositional processes that are presently and have previously operated in the north polar region, and they raise new questions regarding the history of water in the region. In this initial mapping study of the 1.9 μm hydration band depth across the north polar region, we have arrived at the following results and conclusions:

[96] 1. The presence of hydrated minerals in water ice-rich terrains can be detected by exploiting the symmetry of the 2 μm water ice band to estimate the 1.9 μm hydration band depth.

[97] 2. Our results support the *Langevin et al.* [2005a] identification of gypsum in Olympia Planum.

[98] 3. Hydrated minerals are present not just in the dune fields of Olympia Planum, but also in nearly all of the circumpolar erg as well as within Planum Boreum.

[99] 4. The hydrated minerals, and possibly the materials in the circumpolar erg in general, appear to be sourced from Olympia Planum. Thus, the hydration signature in the dune fields outside of Olympia Planum is most likely also due to gypsum. However, other hydrated sulfate-bearing minerals, such as jarosite or ferrihydrite, could also be consistent with some of the observations.

[100] 5. In Planum Boreum, hydrated minerals are present in the dark veneers that emanate from the troughs, and appear to be sourced primarily from the Planum Boreum 2 unit. These materials may have been sourced from the Olympia Planum gypsum deposit in an earlier, more highly erosive epoch.

[101] 6. Our laboratory studies show that variations in the spectrum of gypsum with changes in grain size and abundance can be modeled to estimate the abundance directly from the observed (or estimated) 1.9 μm band depth. Applying these methods to the highest gypsum concentration area in the north polar region yields a maximum abundance of 30 wt % at OMEGA resolutions (at best 1.6 km/pixel in this study), and a maximum abundance of 42 wt % at CRISM resolutions (>18 m/pixel).

[102] 7. The presence of hydrated minerals throughout the Amazonian units of the north polar region implies water activity in the north polar basin during the Amazonian, and suggests that we should carefully consider how and whether the current paradigm for the history of water on Mars applies to the north polar region.

[103] **Acknowledgments.** We thank Ryan Anderson for help with OMEGA mapping tool development, Ken Tanaka for helpful geologic discussions and for providing the base map from his recent geologic mapping paper, and Noel Gorelick for providing a copy of his north polar THEMIS mosaic. We also thank Kathryn Fishbaugh, Alexis Rodriguez, Rob Sullivan, and Peter Thomas for invaluable discussions, comments, and suggestions and two anonymous reviewers for their critical feedback and suggestions on the initial version of this paper. This work was supported by grants from the Mars Data Analysis Program under contracts from NASA, the Mars Odyssey Participating Scientist program under contracts from the Jet Propulsion Laboratory, and the Canadian Space Agency.

References

Bagnold, R. A. (1941), *The Physics of Blown Sand and Desert Dunes*, Methuen Press, London.

Bell, J. F., III, J. F. Wolff, M. J. James, P. B. Clancy, R. T. Lee, and S. W. Martin (1997), Mars surface mineralogy from Hubble Space Telescope imaging during 1994–1995: Observations, calibration, and initial results, *J. Geophys. Res.*, *102*, 9109–9123, doi:10.1029/96JE03990.

Bell, J. F., III, et al. (2004), Pancam multispectral imaging results from the Spirit rover at Gusev Crater, *Science*, *305*, 800–806, doi:10.1126/science.1100175.

Bell, J. F., III, M. S. Rice, J. R. Johnson, and T. M. Hare (2008), Surface albedo observations at Gusev Crater and Meridiani Planum, Mars, *J. Geophys. Res.*, *113*, E06S18, doi:10.1029/2007JE002976.

Bellucci, G., F. Altieri, J. P. Bibring, G. Bonello, Y. Langevin, B. Gondet, and F. Poulet (2006), OMEGA/Mars Express: Visual channel performances and data reduction techniques, *Planet. Space Sci.*, *54*, 675–684, doi:10.1016/j.pss.2006.03.006.

Bibring, J.-P., et al. (2004), OMEGA: Observatoire pour la Minéralogie, lEau, les Glaces et lActivité, in *Mars Express: The Scientific Payload, Eur. Space Agency Spec. Publ., ESA-SP 1240*, pp. 37–49.

Bibring, J.-P., et al. (2005), Mars surface diversity as revealed by the OMEGA/Mars Express observations, *Science*, *307*, 1576–1581, doi:10.1126/science.1108806.

Bibring, J.-P., Y. Langevin, J. F. Mustard, F. Poulet, R. Arvidson, A. Gendrin, B. Gondet, N. Mangold, P. Pinet, F. Forget, and the OMEGA Team (2006), Global mineralogical and aqueous Mars history derived from OMEGA/Mars Express data, *Science*, *312*, 400–404, doi:10.1126/science.1122659.

Bishop, J. L., C. M. Pieters, and R. G. Burns (1993), Reflectance and Mössbauer spectroscopy of ferrihydrite-montmorillonite assemblages as Mars soil analog materials, *Geochim. Cosmochim. Acta*, *57*, 4583–4595, doi:10.1016/0016-7037(93)90184-X.

Blasius, K. R., J. A. Cutts, and A. D. Howard (1982), Topography and stratigraphy of Martian polar layered deposits, *Icarus*, *50*, 140–160, doi:10.1016/0019-1035(82)90122-1.

Bourke, M. C., K. S. Edgett, and B. A. Cantor (2008), Recent aeolian dune change on Mars, *Geomorphology*, *94*, 247–255, doi:10.1016/j.geomorph.2007.05.012.

Burns, R. G. (1987), Ferric sulfates on Mars, *J. Geophys. Res.*, *92*, E570–E574, doi:10.1029/JB092iB04p0E570.

Burns, R. G. (1988), Gossans on Mars, *Proc. Lunar Planet. Sci. Conf.*, *18th*, 713–721.

Burns, R. G., and D. S. Fisher (1990), Iron-sulfur mineralogy of Mars: Magmatic evolution and chemical weathering products, *J. Geophys. Res.*, *95*, 14,415–14,421, doi:10.1029/JB095iB09p14415.

Burns, R. G., and D. S. Fisher (1993), Rates of oxidative weathering on the surface of Mars, *J. Geophys. Res.*, *98*, 3365–3372, doi:10.1029/92JE02055.

Byrne, S., and B. Murray (2002), North polar stratigraphy and the paleo-erg of Mars, *J. Geophys. Res.*, *107*(E6), 5044, doi:10.1029/2001JE001615.

Catling, D. (1999), A chemical model for evaporites on early Mars: Possible sedimentary tracers of the early climate and implications for exploration, *J. Geophys. Res.*, *104*, 16,453–16,470, doi:10.1029/1998JE001020.

Christensen, P. R., J. L. Bandfield, M. D. Smith, V. E. Hamilton, and R. N. Clark (2000), Identification of a basaltic component on the Martian surface from Thermal Emission Spectrometer data, *J. Geophys. Res.*, *105*, 9609–9622, doi:10.1029/1999JE001127.

Christensen, P. R., et al. (2004a), The Thermal Emission Imaging System (THEMIS) for the Mars 2001 Odyssey mission, *Space Sci. Rev.*, *110*, 85–130, doi:10.1023/B:SPAC.0000021008.16305.94.

Christensen, P. R., et al. (2004b), Mineralogy at Meridiani Planum from the Mini-TES experiment on the Opportunity Rover, *Science*, *306*, 1733–1739, doi:10.1126/science.1104909.

Clark, R. N. (1981a), The spectral reflectance of water-mineral mixtures at low temperatures, *J. Geophys. Res.*, *86*, 3074–3086, doi:10.1029/JB086iB04p03074.

Clark, R. N. (1981b), Water frost and ice: The near-infrared spectral reflectance 0.65–2.5 μm, *J. Geophys. Res.*, *86*, 3087–3096, doi:10.1029/JB086iB04p03087.

Clark, R. N., and T. L. Roush (1984), Reflectance spectroscopy: Quantitative analysis techniques for remote sensing applications, *J. Geophys. Res.*, *89*, 6329–6340, doi:10.1029/JB089iB07p06329.

Clark, J. T., J. L. Bishop, M. Parente, A. J. Brown, and N. K. McKeown (2008), Constraining sulfate abundances on Mars using CRISM spectra and laboratory mixtures, *Lunar Planet. Sci.*, *XXXIX*, Abstract 1540.

Cloutis, E. A., et al. (2006), Detection and discrimination of sulfate minerals using reflectance spectroscopy, *Icarus*, *184*, 121–157, doi:10.1016/j.icarus.2006.04.003.

Cloutis, E. A., M. A. Craig, J. F. Mustard, R. V. Kruzelecky, W. R. Jamroz, A. Scott, D. L. Bish, F. Poulet, J. P. Bibring, and P. L. King (2007), Stability of hydrated minerals on Mars, *Geophys. Res. Lett.*, *34*, L20202, doi:10.1029/2007GL031267.

Cooper, C. D., and J. F. Mustard (1999), Effects of very fine particle size on reflectance spectra of smectite and palagonitic soil, *Icarus*, *142*, 557–570, doi:10.1006/icar.1999.6221.

Deer, W. A., R. A. Howie, and J. Zussman (1992), *An Introduction to The Rock-Forming Minerals*, Harlow, Essex, U.K.

Dial, A. L., Jr. (1984), Geologic map of the Mare Boreum area of Mars, scale1:5,000,000, *U.S. Geol. Surv. Misc. Invest. Map*, *I-1640*.

Eckardt, F. D., and R. S. Schemenauer (1998), Fog water chemistry in the Namib Desert, Namibia, *Atmos. Environ.*, *32*, 2595–2599, doi:10.1016/S1352-2310(97)00498-6.

Edgett, K., R. Williams, M. Malin, B. Cantor, and P. Thomas (2003), Mars landscape evolution: Influence of stratigraphy on geomorphology in the north polar region, *Geomorphology*, *52*, 289–297.

Feldman, W. C., et al. (2004), Global distribution of near-surface hydrogen on Mars, *J. Geophys. Res.*, *109*, E09006, doi:10.1029/2003JE002160.

Feldman, W. C., M. C. Bourke, R. C. Elphic, S. Maurice, J. Bandfield, T. H. Prettyman, B. Diez, and D. J. Lawrence (2008), Hydrogen content of sand dunes within Olympia Undae, *Icarus*, *196*, 422–432, doi:10.1016/j.icarus.2007.08.044.

Finkel, H. J. (1959), The barchans of southern Peru, *J. Geol.*, *67*, 614–647.

Fishbaugh, K., and J. Head III (2000), North polar region of Mars: Topography of circumpolar deposits from Mars Orbiter Laser Altimeter (MOLA) data and evidence for asymmetric retreat of the polar cap, *J. Geophys. Res.*, *105*, 22,455–22,486, doi:10.1029/1999JE001230.

Fishbaugh, K., and J. Head III (2001), Comparison of the north and south polar caps of Mars: New observations from MOLA data and discussion of some outstanding questions, *Icarus*, *154*, 145–161, doi:10.1006/icar.2001.6666.

Fishbaugh, K., and J. Head III (2002), Chasma Boreale: Topographic characterization from Mars Orbiter Laser Altimeter data and implications for mechanisms of formation, *J. Geophys. Res.*, *107*(E3), 5013, doi:10.1029/2000JE001351.

Fishbaugh, K., and J. Head III (2005), Origin and characteristics of the Mars north polar basal unit and implications for polar geologic history, *Icarus*, *174*, 444–474, doi:10.1016/j.icarus.2004.06.021.

Fishbaugh, K. E., F. Poulet, V. Chevrier, Y. Langevin, and J. P. Bibring (2007), On the origin of gypsum in the Mars north polar region, *J. Geophys. Res.*, *112*, E07002, doi:10.1029/2006JE002862.

Fryberger, S. G. (2002), *Geological overview of White Sands National Monument*, Online at http://www.nps.gov/whsa/Geology.

Gellert, R., et al. (2004), Chemistry of rocks and soils in Gusev Crater from the Alpha Particle X-Ray Spectrometer, *Science*, *305*, 829–832, doi:10.1126/science.1099913.

Gendrin, A., et al. (2005), Sulfates in Martian layered terrains: The OMEGA/Mars Express view, *Science*, *307*, 1587–1591, doi:10.1126/science.1109087.

Ghrefat, H. A., P. C. Goodell, B. E. Hubbard, R. P. Langford, and R. E. Aldouri (2007), Modeling grain size variations of aeolian gypsum deposits at White Sands, New Mexico, using AVIRIS imagery, *Geomorphology*, *88*, 57–68, doi:10.1016/j.geomorph.2006.10.013.

Golden, D. C., D. W. Ming, R. V. Morris, and S. A. Mertzman (2005), Laboratory-simulated acid-sulfate weathering of basaltic materials: Implications for formation of sulfates at Meridiani Planum and Gusev Crater, Mars, *J. Geophys. Res.*, *110*, E12S07, doi:10.1029/2005JE002451.

Hastenrath, S. L. (1967), The barchans of the Arequipa region, southern Peru, *Z., Geomorphol.*, *11*, 300–311.

Hayward, R. K., L. K. Fenton, K. L. Tanaka, K. F. Mullins, T. N. Titus, M. C. Bourke, T. M. Hare, and P. R. Christensen (2008), Mars global digital dune database: Distribution in north polar region and comparison to equatorial region, *Lunar Planet. Sci.*, *XXXIX*, Abstract 1208.

Herkenhoff, K., and A. Vasavada (1999), Dark material in the polar layered deposits and dunes on Mars, *J. Geophys. Res.*, *104*, 16,487–16,500, doi:10.1029/1998JE000589.

Holland, H. D., and S. D. Malinin (1979), *The solubility and occurrence of non-ore minerals, Geochemistry of Hydrothermal Ore Deposits*, edited by H. L. Barnes, pp. 461–509, John Wiley, New York.

Howard, A., J. Cutts, and K. Blasius (1982), Stratigraphic relationships within Martian polar cap deposits, *Icarus*, *50*, 161–215, doi:10.1016/0019-1035(82)90123-3.

Hunt, G. R., and J. W. Salisbury (1970), Visible and near-infrared spectra of minerals and rocks: I. Silicate minerals, *Mod. Geol.*, *1*, 283–300.

Jambor, J. L., and J. E. Dutrizac (1998), Occurrence and constitution of natural and synthetic ferrihydrite, a widespread iron oxyhydroxide, *Chem. Rev.*, *98*, 2549–2585, doi:10.1021/cr970105t.

Jouglet, D., F. Poulet, R. E. Milliken, J. F. Mustard, J.-P. Bibring, Y. Langevin, B. Gondet, and C. Gomez (2007), Hydration state of the Martian surface as seen by Mars Express OMEGA: 1. Analysis of the 3 (m hydration feature, *J. Geophys. Res.*, *112*, E08S06, doi:10.1029/2006JE002846.

Lancaster, N., and R. Greeley (1990), Sediment volume in the north polar sand seas of Mars, *J. Geophys. Res.*, *95*, 10,921–10,927, doi:10.1029/JB095iB07p10921.

Langevin, Y., F. Poulet, J. P. Bibring, and B. Gondet (2005a), Sulfates in the north polar region of Mars detected by OMEGA/Mars Express, *Science*, *307*, 1584–1586, doi:10.1126/science.1109091.

Langevin, Y., F. Poulet, J.-P. Bibring, B. Schmitt, S. Douté, and B. Gondet (2005b), Summer evolution of the north polar cap of Mars as observed by OMEGA/Mars Express, *Science*, *307*, 1581–1584.

Langevin, Y., M. Vincendon, F. Poulet, J.-P. Bibring, B. Gondet, S. Douté, and T. Encrenaz (2008), Weak signatures of water ice at high northern latitudes: Aerosols, frosts and ice outcrops, *Lunar Planet. Sci.*, *XXXIX*, Abstract 2134.

Langford, R. P. (2003), The Holocene history of the White Sands dune field and influences on eolian deflation and playa lakes, *Quat. Int.*, *104*, 31–39, doi:10.1016/S1040-6182(02)00133-7.

Malin, M., and K. Edgett (2001), Mars Global Surveyor Mars Orbiter Camera: Interplanetary cruise through primary mission, *J. Geophys. Res.*, *106*, 23,429–23,570, doi:10.1029/2000JE001455.

Malin, M. C., et al. (2007), Context Camera investigation onboard the Mars Reconnaissance Orbiter, *J. Geophys. Res.*, *112*, E05S04, doi:10.1029/2006JE002808.

McEwen, A. S., et al. (2007), Mars Reconnaissance Orbiters High Resolution Imaging Science Experiment (HiRISE), *J. Geophys. Res.*, *112*, E05S02, doi:10.1029/2005JE002605.

Milkovich, S., and J. Head III (2005), North polar cap of Mars: Polar layered deposit characterization and identification of a fundamental climate signal, *J. Geophys. Res.*, *110*, E01005, doi:10.1029/2004JE002349.

Milkovich, S., and J. Head III (2006), Surface textures of Mars north polar layered deposits: A framework for interpretation and future exploration, *Mars*, *2*, 21–45.

Milliken, R. E., J. F. Mustard, F. Poulet, D. Jouglet, J.-P. Bibring, B. Gondet, and Y. Langevin (2007), Hydration state of the Martian surface as seen by Mars Express OMEGA: 2. H_2O content of the surface, *J. Geophys. Res.*, *112*, E08S07, doi:10.1029/2006JE002853.

Morris, R. V., and G. Klingelhöfer (2008), Iron mineralogy and aqueous alteration on Mars from the MER Mössbauer Spectrometers, edited by J. F. Bell III, in *The Martian Surface: Composition, Mineralogy, and Physical Properties*, pp. 339–365, Cambridge Univ. Press, Cambridge, U.K.

Morris, R. V., et al. (2006), Mössbauer mineralogy of rock, soil, and dust at Gusev Crater, Mars: Spirits journey through weakly altered olivine basalt on the plains and pervasively altered basalt in the Columbia Hills, *J. Geophys. Res.*, *111*, E02S13, doi:10.1029/2005JE002584.

Noe Dobrea, E. Z., and J. F. Bell III (2001), Composition and mineralogy of the Martian north polar dune deposits: Constraints from TES and HST observations, *Lunar Planet Sci.*, *XXXII*, Abstract 2099.

Pelkey, S. M., et al. (2007), CRISM multispectral summary products: Parameterizing mineral diversity on Mars from reflectance, *J. Geophys. Res.*, *112*, E08S14, doi:10.1029/2006JE002831.

Poulet, F., C. Gomez, J. P. Bibring, Y. Langevin, B. Gondet, P. Pinet, G. Belluci, and J. Mustard (2007), Martian surface mineralogy from Observatoire pour la Minéralogie, lEau, les Glaces et lActivité on board the Mars Express spacecraft (OMEGA/MEx): Global mineral maps, *J. Geophys. Res.*, *112*, E08S02, doi:10.1029/2006JE002840.

Roach, L., et al. (2007), CRISM spectral signatures of the north polar gypsum dunes, *Lunar Planet Sci.*, *XXXVII*, Abstract 1970.

Rodriguez, J. A. P., K. L. Tanaka, Y. Langevin, M. Bourke, J. Kargel, P. Christensen, and S. Sasaki (2007), Recent aeolian erosion and deposition in the north polar plateau of Mars, *Mars*, *3*, 29–41.

Rogers, A. D., and O. Aharonson (2008), Mineralogical composition of sands in Meridiani Planum determined from MER data and comparison to orbital measurements, *J. Geophys. Res.*, *113*, E06S14, doi:10.1029/2007JE002995.

Roush, T. L., J. B. Pollack, F. C. Witteborn, J. D. Bregman, and J. P. Simpson (1990), Ice and minerals on Callisto: A reassessment of the reflectance spectra, *Icarus*, *86*, 355–382, doi:10.1016/0019-1035(90)90225-X.

Roush, T. L., F. Esposito, G. R. Rossman, and L. Colangeli (2007), Estimated optical constants of gypsum in the regions of weak absorptions: Application of scattering theories and comparisons to independent measurements, *J. Geophys. Res.*, *112*, E10003, doi:10.1029/2007JE002920.

Ruff, S. W., and P. R. Christensen (2007), Basaltic andesite, altered basalt, and a TES based search for smectite clay minerals on Mars, *Geophys. Res. Lett.*, *34*, L10204, doi:10.1029/2007GL029602.

Sagan, C., D. Pieri, P. Fox, R. E. Arvidson, and E. A. Guinness (1977), Particle motion on Mars inferred from the Viking lander cameras, *J. Geophys. Res.*, *82*, 4430–4438, doi:10.1029/JS082i028p04430.

Schatz, V., H. Tsoar, K. S. Edgett, E. J. R. Parteli, and H. J. Herrmann (2006), Evidence for indurated sand dunes in the Martian north polar region, *J. Geophys. Res.*, *111*, E04006, doi:10.1029/2005JE002514.

Schreiber, B. C., and M. El Tabakh (2000), Deposition and early alteration of evaporites, *Sedimentology*, *47*, 215–238, doi:10.1046/j.1365-3091.2000.00002.x.

Scott, D. H., and M. H. Carr (1978), Geologic map of Mars, scale1:25,000,000, *U.S. Geol. Surv. Misc. Invest. Map*, *I-1083*.

Scott, D. H., and K. L. Tanaka (1987), Geologic map of the polar regions of Mars, scale1:15,000,000,000, *U.S. Geol. Surv. Misc. Invest. Map*, *I-1802-C*.

Seelos, F., S. Murchie, S. Pelkey, K. Seelos, and the CRISM Team (2007), CRISM multispectral survey campaign—Status and initial mosaics, *Lunar Planet. Sci.*, *XXXIX*, Abstract 2336.

Smith, D. E., et al. (2001), Mars Orbiter Laser Altimeter: Experiment summary after the first year of global mapping of Mars, *J. Geophys. Res.*, *106*, 23,689–23,722, doi:10.1029/2000JE001364.

Soderblom, J. M., J. F. Bell III, M. Y. Hubbard, and M. J. Wolff (2006), Martian phase function: Modeling the visible to near-infrared surface photometric function using HST-WFPC2 data, *Icarus*, *184*, 401–423, doi:10.1016/j.icarus.2006.05.006.

Spencer, R. J. (2000), Sulfate minerals in evaporite deposits, *Rev. Mineral. Geochem.*, *40*, 173–192.

Stoiber, R. E., and W. I. Rose Jr. (1974), Fumarole incrustations at active central American volcanoes, *Geochim. Cosmochim. Acta*, *38*, 495–516, doi:10.1016/0016-7037(74)90037-4.

Sullivan, R., et al. (2008), Wind-driven particle mobility on Mars: Insights from MER observations at "El Dorado" and surroundings at Gusev Crater, *Lunar Planet. Sci.*, *XXXIX*, Abstract 2092.

Tanaka, K. (2005), Geology and insolation-driven climatic history of Amazonian north polar materials on Mars, *Nature*, *437*, 991–994, doi:10.1038/nature04065.

Tanaka, K. L. (2006), North polar gypsum: Possible origin related to early Amazonian volcanisms at Alba Patera and aeolian mining, paper presented at 4th International Conference on Mars Polar Science and Exploration, Lunar Planet. Inst., Davos, Switzerland.

Tanaka, K. L., and R. K. Hayward (2008), Mars north circum-polar dunes: Distribution, sources, and migration history, paper presented at Planetary Dunes Workshop, Lunar Planet. Inst., Alamogordo, N. M.

Tanaka, K. L., J. Skinner Jr., T. Hare, T. Joyal, and A. Wenker (2003), Resurfacing history of the northern plains of Mars based on geologic mapping of Mars Global Surveyor data, *J. Geophys. Res.*, *108*(E4), 8043, doi:10.1029/2002JE001908.

Tanaka, K. L., J. A. P. Rodriguez, J. A. Skinner Jr., M. C. Bourke, C. M. Fortezzo, K. E. Herkenhoff, E. J. Kolb, and C. H. Okubo (2008), North polar region of Mars: Advances in stratigraphy, structure, and erosional modification, *Icarus*, *196*, 318–358, doi:10.1016/j.icarus.2008.01.021.

Thomas, P., and C. Weitz (1989), Sand dune materials and polar layered deposits on Mars, *Icarus*, *81*, 185–215, doi:10.1016/0019-1035(89)90133-4.

Tsoar, H., R. Greeley, and A. Peterfreund (1979), Mars: The north polar sand sea and related wind patterns, *J. Geophys. Res.*, *84*, 8167–8180, doi:10.1029/JB084iB14p08167.

Vincent, P. J. (1984), Particle size variation over a transverse dune in the Nafud as Sirr, central Saudi Arabia, *J. Arid Environ.*, *7*, 329–336.

Warner, N. H., and J. D. Farmer (2007), Importance of aeolian processes in the origin of the north polar chasmata, Mars, *Icarus*, *196*, doi:10.1016/j.icarus.2007.08.043.

Warren, J. K. (1982), The hydrological setting, occurrence and significance of gypsum in late Quaternary salt lakes in South Australia, *Sedimentology*, *29*, 609–637, doi:10.1111/j.1365-3091.1982.tb00071.x.

Watson, A. (1986), Grain size variations on a longitudinal dune and a barchan dune, *Sediment. Geol.*, *46*, 49–66, doi:10.1016/0037-0738(86)90005-9.

Wyatt, M. B. (2007), The chemically altered basaltic northern plains of Mars: TES, OMEGA, and GRS integrated data sets and conclusions, paper presented at Seventh International Conference on Mars, Lunar Planet. Inst., Pasadena, Calif.

Wyatt, M. B., H. McSween Jr., K. Tanaka, and J. Head III (2004), Global geologic context for rock types and surface alteration on Mars, *Geology*, *32*, 645–648, doi:10.1130/G20527.1.

Zuber, M. T., D. E. Smith, S. C. Solomon, D. O. Muhleman, J. W. Head, J. B. Garvin, J. B. Abshire, and J. L. Bufton (1992), The Mars Observer laser altimeter investigation, *J. Geophys. Res.*, *97*, 7781–7797.

Zuber, M. T., et al. (1998), Observations of the north polar region of Mars from the Mars Orbiter Laser Altimeter, *Science*, *282*, 2053–2060, doi:10.1126/science.282.5396.2053.

D. T. Bailey, E. A. Cloutis, and M. A. Craig, Department of Geography, University of Winnipeg, Winnipeg, MB R3B 2E9, Canada.

J. F. Bell III and B. H. Horgan, Department of Astronomy, Cornell University, Ithaca, NY 14853, USA.

J. F. Mustard and H. Roach, Department of Geological Sciences, Brown University, Providence, RI 02912, USA.

E. Z. Noe Dobrea, JPL, California Institute of Technology, Pasadena, CA 91109, USA.